**Article:**
Dogan, H., Sims, N.D. and Wagg, D.J. (2022) Design, testing and analysis of a pivoted-bar inerter device used as a vibration absorber. Mechanical Systems and Signal Processing, 171. 108893. ISSN: 0888-3270

https://doi.org/10.1016/j.ymssp.2022.108893

# Highlights

## Design, testing and analysis of a pivoted-bar inerter device used as a vibration absorber

Hakan Dogan,Neil D. Sims,David J. Wagg

- A new design for an inerter-based dynamic vibration absorber (IDVA) is developed, which can be deployed between an auxiliary mass and a host structure.
- A pivoted-bar mechanism with frictionless flexure hinges is used for the physical realisation of the inerter device.
- The inerter device designed allows fine tuning of the inertance by simply adding additional masses.
- Hysteretic damping is employed in the proposed device.
- The vibration suppression performance improvement is experimentally validated and performs 18% better than a classical tuned mass damper.

# Design, testing and analysis of a pivoted-bar inerter device used as a vibration absorber

Hakan Dogan*, Neil D. Sims and David J. Wagg

*Department of Mechanical Engineering, The University of Sheffield, S1 3JD, Sheffield, UK*

ARTICLE INFO

*Keywords*:
Passive vibration control
Inerter
Experimental study
Inerter-based absorber
Tuned inerter damper

ABSTRACT

In this paper a new design for a small scale inerter-based dynamic vibration absorber (IDVA) is presented, based upon a pivoted-bar mechanism. There are several new innovations in this study. The first is to design, build and test an inerter-based device that does not need to be grounded, or placed between different parts of the structure in order to create relative motion. Instead, the relative motion is created between an auxiliary mass and the host structure. Secondly, the pivoted-bar mechanism is designed to act as a pure inerter, and avoids unbalanced inertance effects such as those that occur in the dynamic antiresonant vibration isolator (DAVI). Thirdly, the effects of parasitic mass are minimised by using (i) the appropriate device arrangements, (ii) numerical optimisation, and (iii) fine tuning of the device by adding small additional masses. Fourth, the optimum device damping values are obtained by using a gel damper that can be modelled as a hysteretic damper. In addition, the design uses frictionless flexure hinges that have a small amount of stiffness that can affect the device performance. It is shown how this can also be compensated for using the design optimisation and fine tuning strategies. Detailed design and analysis methodologies are provided, in order to extend the existing work on inerters towards practical design and implementation. In terms of applications, it is anticipated that the design would be suitable for small-size restricted-space applications. A prototype of the design for a small-scale and relatively high frequency application is manufactured. Experimental and numerical results show that the device provides a 18% improvement in performance compared to a classical tuned mass damper (TMD).

## 1. Introduction

Inerter-based devices have been increasingly utilised in recent years to mitigate the effects of unwanted vibrations in machines and structures. An inerter is a mechanical device that generates a force proportional to the relative acceleration between its terminals. The concept was introduced by Smith [1] in 2002 using the force-current analogy between mechanical and electrical systems.

Prior to Smith's work, multiple other mechanical devices had been used as inerters, but were known by other names — see for example the historical review in [2]. For example, an inerter device called the gyro-mass was patented by Atsushi [3] in 1997. Similarly, a relative-acceleration inertial mechanism, named the rotational-viscous-damper, was studied by Kuroda et al. [4] and Saito et al. [5]. Later, Ikago [6] proposed the tuned-viscous-mass-damper (TVMD) by adding a flywheel and a spring to the rotational-viscous-damper.

One aspect of inerter research that has received much attention is the performance of devices with different configurations of elements (normally springs, viscous dampers, inerters and masses). From this, three main configurations have emerged as most commonly used. The first is the TVMD [6], mentioned above. The second, proposed by Lazar et al. [7], is the tuned-inerter-damper (TID). The TID is broadly similar to a classical tuned-mass-damper (TMD), but with inertance replacing the mass element. The TID parameter design (known as tuning) initially followed an iterative strategy based on the fixed-points theory of Den Hartog [8]. Hu et al. [9] systematically evaluated performance of five different inerter-based configurations for both isolation and absorption applications (note the TID was labelled C3 in their study). The authors obtained closed-form solutions for the optimal design parameters for both $H_\infty$ and $H_2$ performances of the inerter-based isolators considered.

The third important device configuration was proposed by Marian and Giaralis [10, 11] and is called the tuned-mass-damper-inerter (TMDI). The authors derived the closed-form solution for the optimal design parameters for an

*Corresponding author
hdogan1@sheffield.ac.uk (H. Dogan); n.sims@sheffield.ac.uk (N.D. Sims); david.wagg@sheffield.ac.uk (D.J. Wagg)
ORCID(s): 0000-0002-6523-7290 (H. Dogan); 0000-0002-6292-6736 (N.D. Sims); 0000-0002-7266-2105 (D.J. Wagg)

undamped single degree-of-freedom (SDOF) system equipped with a TMDI under harmonic excitation and compared vibration suppression performance to a TMD. Similar to the TID, a TMDI can reduce the mass of the device without loss in the control performance when compared with the TMD. Alternatively the TMDI can achieve a better suppression performance than the TMD for the same sized mass. The performance of TMDI was further discussed in [12] by employing a generic model and in [13] by considering the nonlinear response.

Further studies of the (passive) control performance of these devices have been undertaken. For example, Hu and Chen [14] investigated the $H_\infty$ and $H_2$ performances of an undamped SDOF system controlled by six different configurations of inerter-based dynamic vibration absorbers (IDVAs). The IDVAs in their study are built by replacing the damper element in the TMD with inerter-based mechanical networks, including the TID (as IDVA-C4) and TVMD (as IDVA-C6). It was demonstrated that employing an inerter with a spring to a TMD improves the performance by more than 20% for small mass ratios and provides a wider effective frequency range. Barredo et al. [15] extended the fixed-points theory (mentioned above) to derive quasi-optimal design parameters for a $H_\infty$ optimisation of the best performing devices which were the TID (C4 in [14]) and TVMD (C6 in [14]). Inspired by the work of Zhou et al. [16], Barredo et al. [17] subsequently proposed using these configurations physically attached to a TMD connecting the host structure and the supporting ground. Their study demonstrated that a grounded TID connected to a TMD further improves both the $H_\infty$ and $H_2$ performances for an undamped SDOF system. However, as is also the case for the TMDI, a grounded connection limits the possible layouts for multi-degree-of-freedom structures.

Applications of TID and TMDI with non-grounded inerters were analysed in different studies, including the initial works [7, 10] and in studies regarding wind-induced vibration control of structures [18, 19] and seismic control [20]. Similarly, TVMD application with a non-grounded inerter is also possible [21]. Furthermore, more complex layouts with non-grounded inerters were presented for vehicle suspension systems [22]. However, all these non-grounded inerter applications are deployable between two different parts of the structure (e.g. between two adjacent storey or between vehicle body and tyre) to create relative motion. Although these layouts have the potential of providing better performance than a classical TMD, they do not provide as versatile solution as TMDs. IDVAs, on the other hand, are identical to TMDs in terms of implementation. They are attached to a host structure with an auxiliary mass instead of placing between two different parts of the structure. Although their performances were theoretically studied [14, 23, 24], to the author's knowledge, no experimental study has been conducted. The physical realisation of an IDVA for experimental study requires a special attention in its design, especially in small-scale applications. Therefore, this study addresses a small-scale design of an IDVA and experimental validation of its performance.

In terms of application areas, inerters have been proposed for vehicle suspension systems [22, 25, 26, 27], motorcycle steering [28], building isolation [7, 29, 30, 31], landing-gear systems in aircraft [32], train suspensions [33], wind turbines [23] and large-space applications [34, 35, 36]. In terms of practical design, the most common types are the rack and pinion inerter [1, 37], the ball-screw inerter [37], and fluid-based inerters [34, 31]. More detailed discussions of some mechanical inerter devices are described in [38].

The impacts of friction that exists in the rack and pinion inerter [13, 25], the ball-screw inerter [39], and the fluid-based inerter [40] has been explored. However, the majority of inerter systems have been proposed for relatively large-scale applications, and as a mechanical device gets smaller, friction between components and flow losses (for fluid-based devices) can become increasingly problematic. To the author's knowledge, the only inerter design which has been developed for use in applications of a smaller-scale was the recently proposed frictionless, living-hinge inerter [41], where the device size was of the order of 120mm. This device used a pivoted flywheel inerter design, whilst simultaneously eliminating friction by using flexural-hinges (living-hinges) at the pivots. This inerter was used in an isolator system where one terminal of the inerter is grounded (or connected to an infinitely large mass). The rigid body motion of the inerter can therefore be neglected in their study.

This study proposes a new mechanical design of an IDVA which uses a pivoted-bar mechanism with flexural-hinges and is of a similar scale to the device studied in [41] but includes the rigid body motion of the inerter by considering the mass of the inerter. Therefore, one novel aspect of the new design is that is can be mounted at a specific point on the host structure, in the same manner as a classical TMD. This is in contrast to most inerter applications which have to be either grounded, or positioned between host system components to work effectively. The design is experimentally validated for the vibration suppression of an forced-excited SDOF system. In this context, it offers an experimental validation of the performance improvement of an IDVA-C4 (in [14]). Another novelty in the inerter designed in this study, which is based on a modified version of the pivoted flywheel inerter design of John and Wagg [41], is that it allows the adjustment of its inertance by simply attaching additional lumped masses. This feature is particularly useful for fine tuning of the inertance after manufacture. Linear hysteretic damping is used in the experimental system,

following the work of Deastra et al. [42]. Many previous studies concerning inerter configurations have tended to focus on lumped parameter analysis of the system performance. Therefore, one final aim of the present study is to provide a more detailed design methodology to support the implementation of the approach in practice. It is worth noting that small angle approximation is applied to establish the linear model in the design study of the pivoted-bar inerter. Large relative motion of the pivoted-bar violates this approximation and would introduce nonlinearity in the model.

Performance improvement through the use of an idealised (i.e. theoretical) IDVA has already been shown for an undamped system in [14]. However, for relatively small scale applications, the physical realisation of an idealised IDVA can be impracticable. Consideration of a parasitic mass and hysteretic damping in the model can be favourable in terms of practicality. Therefore, Section 2 presents performance evaluations of the IDVA with a parasitic mass, and the IDVA with both a parasitic mass and hysteretic damping by comparing the idealised IDVA. This includes using the self-differential evolution (SaDE) algorithm to obtain the optimal device parameters to meet the required performance specification. Then in Section 3 the detail of the IDVA device design with a pivoted-bar inerter is presented. This includes the design of the flexure notches used in the design of pivots. The effect of the stiffness on the flexure notch and the fatigue life cycle are also evaluated in this Section. Furthermore, the damping and the stiffness of the silicone gel used in the physical device is characterised. In Section 4, experimental test results are presented in order to validate the design and analysis undertaken in the preceding sections. Finally discussions and conclusions are presented in Sections 5 and 6 respectively.

## 2. Mathematical models and performance analyses

### 2.1. Mathematical models

A schematic representation of a damped SDOF system with three types of IDVA is shown in Figure 1. Throughout the paper, the three cases shown in Figure 1 will be referred to as designs D1, D2, and D3. The IDVAs are obtained by replacing the damper element in a classical TMD with an inerter-based mechanical network (denoted in Figure 1 by a blue dashed-circle), which is the only part that differs in each design. The damped SDOF subsystem is the host structure which is subject to unwanted vibrations, and has parameters, mass $M$ kg, spring stiffness, $K$ N/m, and viscous damping, $C$ Ns/m. The designs D1, D2, and D3 are mounted on the host structure and denoted in Figure 1 by a dashed-box. Each of the three designs has a mass $m_a$ kg and spring $k_o$ N/m, and a series of other components including; inerter, $b$ kg, parasitic mass $m_p$ kg, viscous damper $c$ Ns/m, spring $k_i$ N/m and hysteretic spring/damper $k_i(1+j\eta)$ N/m, where $\eta$ is the loss factor and $j=\sqrt{-1}$. These components are all localised additions [43] to the host structure; as previously noted this is an important feature of the proposed design configurations, as the designs do not require structural connections to the ground.

The logic linking the three designs is that D1, shown in Figure 1 (a), corresponds to an idealised (i.e. theoretical) TID, which is the concept from which the practical design is derived. However, to implement an TID in practice some additional factors have to be taken into account. Firstly, parasitic mass (explained below) needs to be included, and so D2 (Figure 1 (b)) is the same as D1, but with the addition of a parasitic mass, $m_p$. Secondly, the practical damping used is a hysteretic gel damper, and thus in D3, a hysteretic damper is modelled. Note that D2 is similar to the TMDI studied by [10], and D3 is similar to the tuned-mass-hysteretic-damper-inerter (TMhDI) considered in [42], but with a design approach that assumes an addition of the absorber subsystem (dashed boundary in Figure 1), rather than modifications to the bracing or inter-storey compliance of an existing lumped parameter system.

The issue of parasitic mass arises because in smaller-scale applications of this type, the possible inertance-to-mass ratios ($\delta = b/m_a$) are relatively small, specifically $0.01 < \mu < 0.1$ in this study. Because $\delta$ is small, the mass of other components in the system can act as parasitic mass and distort the overall performance. Therefore, when tuning the inertance value for optimum performance the parasitic mass needs to be considered — as discussed in [44]. For example, in Section 3.3 it will be shown that the mass of the sliding plate moving in the hysteretic gel damper acts as a parasitic mass in the system.

The equations of motion of the SDOF system controlled with D1, shown in Figure 1a, can be derived as

$$\begin{aligned} &M\ddot{x}_m(t) + C\dot{x}_m(t) + Kx_m(t) - k_o\big(x_a(t) - x_m(t)\big) - F_{TID}(t) = F(t),\\ &m_a\ddot{x}_a(t) + k_o\big(x_a(t) - x_m(t)\big) + F_{TID}(t) = 0,\\ &F_{TID}(t) = b\big(\ddot{x}_b(t) - \ddot{x}_m(t)\big) = c\big(\dot{x}_a(t) - \dot{x}_b(t)\big) + k_i\big(x_a(t) - x_b(t)\big), \end{aligned} \tag{1}$$

where $x_m(t)$ and $x_a(t)$ are the displacements of the host structure and the auxiliary mass, respectively and $x_b(t)$ is the

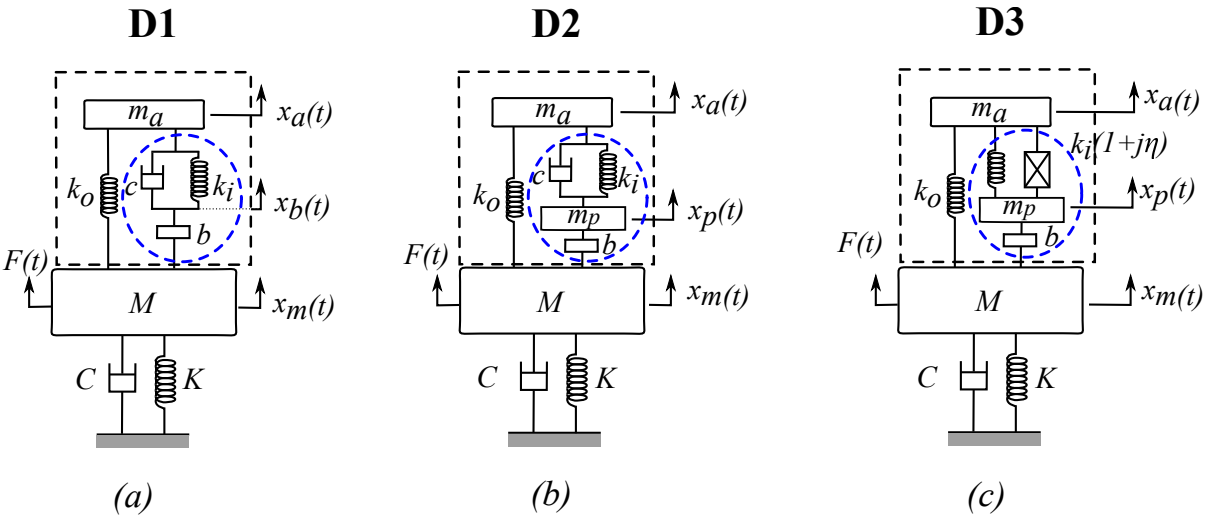


**Figure 1**: Schematic diagram showing the IDVA with three mechanical network designs for a SDOF host structure that is subject to unwanted vibrations. The mechanical network design acts in parallel with a spring and is denoted by a blue dashed-circle. Specifically: (a) D1, the idealised configuration based on a TID [7], (b) D2, as for D1 but with a parasitic mass added, and (c) D3, as for D2 but with a hysteretic damper added.

displacement of the point between the inerter and the spring-damper arrangement, as shown in Figure 1 (a). Meanwhile, $M$, $m_a$ are the host and absorber masses, $C$ and $K$ are the stiffness and damping of the host system, $k_o, k_i, c$ & $b$ are the stiffnesses of the outer spring and the inner spring, damping of the absorber and the inertance of the inerter respectively. $F(t)$ and $F_{TID}(t)$ are the excitation force and the force which is transmitted across the terminals of the series-connected inerter to the spring-damper arrangement.

Similarly, the equations of motion for the mechanical model D2 (Figure 1 (b)) can be derived as

$$\begin{aligned} &M\ddot{x}_m(t) + C\dot{x}_m(t) + Kx_m(t) - b\big(\ddot{x}_p(t) - \ddot{x}_m(t)\big) - k_o\big(x_a(t) - x_m(t)\big) = F(t), \\ &m_p\ddot{x}_p(t) + b\big(\ddot{x}_p(t) - \ddot{x}_m(t)\big) - c\big(\dot{x}_a(t) - \dot{x}_p(t)\big) - k_i\big(x_a(t) - x_p(t)\big) = 0, \\ &m_a\ddot{x}_a(t) + k_o\big(x_a(t) - x_m(t)\big) + c\big(\dot{x}_a(t) - \dot{x}_p(t)\big) + k_i\big(x_a(t) - x_p(t)\big) = 0, \end{aligned} \tag{2}$$

where $m_p$ is the parasitic mass positioned between the inerter and the spring-damper, and $x_p(t)$ is the displacement of the parasitic mass.

The following dimensionless parameters are now introduced:

$$\begin{aligned} &\mu = \frac{m_a}{M}, \quad \beta = \frac{m_p}{m_a}, \quad \delta = \frac{b}{m_a}, \quad \zeta_m = \frac{C}{2\sqrt{KM}}, \\ &\Omega = \frac{\omega}{\omega_m}, \quad \gamma = \frac{\omega_a}{\omega_m}, \quad \alpha = \frac{\omega_b}{\omega_a}, \quad \zeta_a = \frac{c}{2\sqrt{k_o m_a}}, \end{aligned} \tag{3}$$

where $\omega$ is the forcing frequency and $\omega_m, \omega_a$ and $\omega_b$ can be expressed as

$$\omega_m = \sqrt{\frac{K}{M}}, \qquad \omega_a = \sqrt{\frac{k_o}{m_a}}, \qquad \omega_b = \sqrt{\frac{k_i}{b}}.$$

Taking the Fourier transform of Equations 1 and 2, dimensionless versions of the equations of motion can be written

in the frequency domain. From Equation 1, the equations of motion for D1 can be derived as

$$\begin{aligned}&\Big[\delta\Omega^4 - j2\left(\zeta_m\delta + \zeta_a\gamma\left(1+\mu\delta\right)\right)\Omega^3 - \left(4\zeta_m\zeta_a\gamma + \delta + \alpha^2\gamma^2\delta\left(1+\mu\delta\right)\right)\Omega^2\\&+ j2\left(\zeta_m\alpha^2\gamma^2\delta + \zeta_a\gamma\left(1+\mu\gamma^2\right)\right)\Omega + \left(\alpha^2\gamma^2\delta\left(1+\mu\gamma^2\right)\right)\Big]X_m\left(\Omega\right) + \Big[j2\zeta_a\mu\gamma\delta\Omega^3\\&+ \left(\mu\gamma^2\delta\left(1+\alpha\delta\right)\right)\Omega^2 - j2\zeta_a\mu\gamma^3\Omega - \mu\gamma^4\alpha^2\delta\Big]X_a\left(\Omega\right) = \Delta\left(\Omega\right)\left(-\delta\Omega^2 + j2\gamma\zeta_a\Omega + \alpha^2\gamma^2\delta\right),\end{aligned} \tag{4}$$

$$\begin{aligned}&\Big[j2\zeta_a\gamma\delta\Omega^3 + \left(\gamma^2\delta\left(1+\gamma^2\delta\right)\right)\Omega^2 - j2\zeta_a\gamma^3\Omega - \gamma^4\alpha^2\delta\Big]X_m\left(\Omega\right) + \Big[\delta\Omega^4 - j2\left(\zeta_a\gamma\left(1+\delta\right)\right)\Omega^3\\&- \left(\gamma^2\delta\left(\alpha^2+1+\delta\right)\right)\Omega^2 + j2\zeta_a\gamma^3\Omega + \gamma^4\alpha^2\delta\Big]X_a\left(\Omega\right) = 0,\end{aligned}$$

where $X_m(\Omega)$ and $X_a(\Omega)$ are the Fourier transforms of $x_m(t)$ and $x_a(t)$. $\Delta(\Omega) = \mathcal{F}\{F(t)\}/K$ is the scaled excitation signal in the frequency domain. The equivalent equations of motion for D2 are obtained from Equation 2 as

$$\begin{aligned}&\left(\left(-1-\delta\mu\right)\Omega^2 + i2\zeta_m\Omega + 1 + \gamma^2\mu\right)X_m\left(\Omega\right) + \left(\delta\mu\Omega^2\right)X_p\left(\Omega\right) - \left(\gamma^2\mu\right)X_a\left(\Omega\right) = \Delta\left(\Omega\right),\\&\left(\delta\Omega^2\right)X_m\left(\Omega\right) + \left(\left(-\delta-\beta\right)\Omega^2 + i2\zeta_a\gamma\Omega + \alpha^2\gamma^2\delta\right)X_p\left(\Omega\right) + \left(-j2\zeta_a\gamma\Omega - \alpha^2\gamma^2\delta\right)X_a\left(\Omega\right) = 0,\\&\left(-\gamma^2\right)X_m\left(\Omega\right) + \left(-j2\zeta_a\gamma\Omega - \alpha^2\gamma^2\delta\right)X_p\left(\Omega\right) + \left(-\Omega^2 + j2\zeta_a\gamma\Omega + \gamma^2 + \alpha^2\gamma^2\delta\right)X_a\left(\Omega\right) = 0,\end{aligned} \tag{5}$$

where $X_p(\Omega)$ is the Fourier transform of the displacement of $x_p(t)$.

The imaginary part in the complex stiffness term in D3 has no physical meaning in the time domain and this leads to a noncausal model. The time domain analysis of this model can be important for the problem where the transient response of the system is critical such as seismic response of a structure [42]. One method to obtain the time-domain response using analytic signals was presented by Inaudi and Makris [45] and extended to the TID and the TMDI with hysteretic damping by Deastra et al. [42]. However, the scope of the present study is only the steady-state response. For the steady-state response, the equations of motion for D3 can be directly expressed in the frequency domain. Taking $c = 0$ and replacing the stiffness $k_i$ term with complex stiffness term $k_i(1 + j\eta)$ in D2 the equations of motion for the mechanical model D3 (Figure 1 (c)) can be written as

$$\begin{aligned}&-\omega^2 M X_m\left(\omega\right) + j\omega C X_m\left(\omega\right) + K X_m\left(\omega\right) + \omega^2 b\left(X_p\left(\omega\right) - X_m\left(\omega\right)\right) - k_o\left(X_a\left(\omega\right) - X_m\left(\omega\right)\right) = F\left(\omega\right),\\&-\omega^2 m_p X_p\left(\omega\right) - \omega^2 b\left(X_p\left(\omega\right) - X_m\left(\omega\right)\right) - k_i\left(1+j\eta\right)\left(X_a\left(\omega\right) - X_p\left(\omega\right)\right) = 0,\\&-\omega^2 m_a X_a\left(\omega\right) + k_o\left(X_a\left(\omega\right) - X_m\left(\omega\right)\right) + k_i\left(1+j\eta\right)\left(X_a\left(\omega\right) - X_p\left(\omega\right)\right) = 0.\end{aligned} \tag{6}$$

Using the dimensionless parameters in Equation 3, the dimensionless form of the equations of motion for D3 are written from Equation 6 as

$$\begin{aligned}&\left(\left(-1-\delta\mu\right)\Omega^2 + j2\zeta_m\Omega + 1 + \gamma^2\mu\right)X_m\left(\Omega\right) + \left(\delta\mu\Omega^2\right)X_p\left(\Omega\right) - \left(\gamma^2\mu\right)X_a\left(\Omega\right) = \Delta\left(\Omega\right),\\&\left(\delta\Omega^2\right)X_m\left(\Omega\right) + \left(\left(-\delta-\beta\right)\Omega^2 + \alpha^2\gamma^2\delta\left(1+j\eta\right)\right)X_p\left(\Omega\right) - \left(\alpha^2\gamma^2\delta\left(1+j\eta\right)\right)X_a\left(\Omega\right) = 0,\\&\left(-\gamma^2\right)X_m\left(\Omega\right) - \left(\alpha^2\gamma^2\delta\left(1+j\eta\right)\right)X_p\left(\Omega\right) + \left(-\Omega^2 + \gamma^2 + \alpha^2\gamma^2\delta\left(1+j\eta\right)\right)X_a\left(\Omega\right) = 0.\end{aligned} \tag{7}$$

With some algebraic manipulation, it is possible to define the dimensionless frequency response functions between the host structure and the excitation force:

$$|H_{D1}(\Omega,\delta,\gamma,\alpha,\zeta_a,\zeta_m,\mu)| = \frac{X_m}{\Delta}, \tag{8}$$

$$|H_{D2}(\Omega,\delta,\gamma,\alpha,\beta,\zeta_a,\zeta_m,\mu)| = \frac{X_m}{\Delta}, \tag{9}$$

$$|H_{D3}(\Omega,\delta,\gamma,\alpha,\beta,\eta,\zeta_m,\mu)| = \frac{X_m}{\Delta}. \tag{10}$$

Full expressions for Equations 8-10 are given in Appendix A. The dimensionless FRFs derived from Equations 8-10 are used in the numerical optimisation to obtain the optimal design parameters which is considered next.

| | $\mu$ | $\beta$ | $\gamma$ | $\alpha$ | $\delta$ | $\zeta_a$ | $\eta$ |
|---|---|---|---|---|---|---|---|
| TMD | 0.0474 | – | 0.9476 | – | – | 0.1342 | – |
| D1 | 0.0474 | – | 0.9710 | 0.9413 | 0.1073 | 0.0224 | – |
| D2 | 0.0450 | 0.054 | 0.9993 | 1.2924 | 0.0559 | 0.0221 | – |
| D3 | 0.0450 | 0.054 | 0.9870 | 1.2209 | 0.0655 | – | 0.5114 |

**Table 1**
Optimal dimensionless design parameters for the IDVAs and TMD.

## 2.2. Tuning strategy and optimisation

To minimise the maximum amplitude, $H_\infty$ optimisation is used to obtain the optimal design parameters. For an undamped SDOF host structure controlled with D1, closed-form solutions for the quasi-optimal design parameters were presented in [15] and the optimal design parameters were already numerically obtained in [14]. However, these optimal parameters are only applicable to undamped SDOF structures. Here, the optimal design parameters of D1 will be determined by considering the damping in the host structure and the optimal design parameters of each configuration will be numerically obtained using the Self-adaptive Differential Evolution (SaDE) algorithm [46, 47].

To do this, the objective function for $H_\infty$ optimisation will be constructed as follows

$$\min_{\chi}\Big(\max_{\Omega}\big(|H_i(\Omega)|\big)\Big), \tag{11}$$

where $\chi$ is a vector containing the unknown design parameters of the $i$th design, $\mathrm{D}_i$, for $i = 1, 2, 3$. Therefore, the design parameters vector becomes $\chi = [\delta, \gamma, \alpha, \zeta_a]^T$ for D1 and D2, and $\chi = [\delta, \gamma, \alpha, \eta]^T$ for D3. The function $|H_i(\Omega)|$ is given in Equations 8-10 for D1, D2 & D3 respectively. It is assumed that Equation 11 is subjected to $\chi > 0$ as each parameter has to be a real and positive value.

For a given mass ratio, $\mu$, and parasitic mass ratio, $\beta$, the dimensionless optimal design parameters computed using the SaDE algorithm are given in Table 1. In order to try and make a fair comparison of the performance analysis, the inertial effect of the parasitic mass in D2 and D3 was also included in D1 and the TMD cases, by taking the sum of $m_p$ and $m_a$ as the auxiliary mass. Therefore, an equivalent mass ratio, which equals $\mu_{\mathrm{D3}}(1 + \beta_{\mathrm{D3}})$, was considered for D1 and the TMD. The frequency response of each configuration is shown in Figure 2 in comparison with a TMD and the uncontrolled host structure. The result shows that D2 and D3 provide almost identical vibration suppression

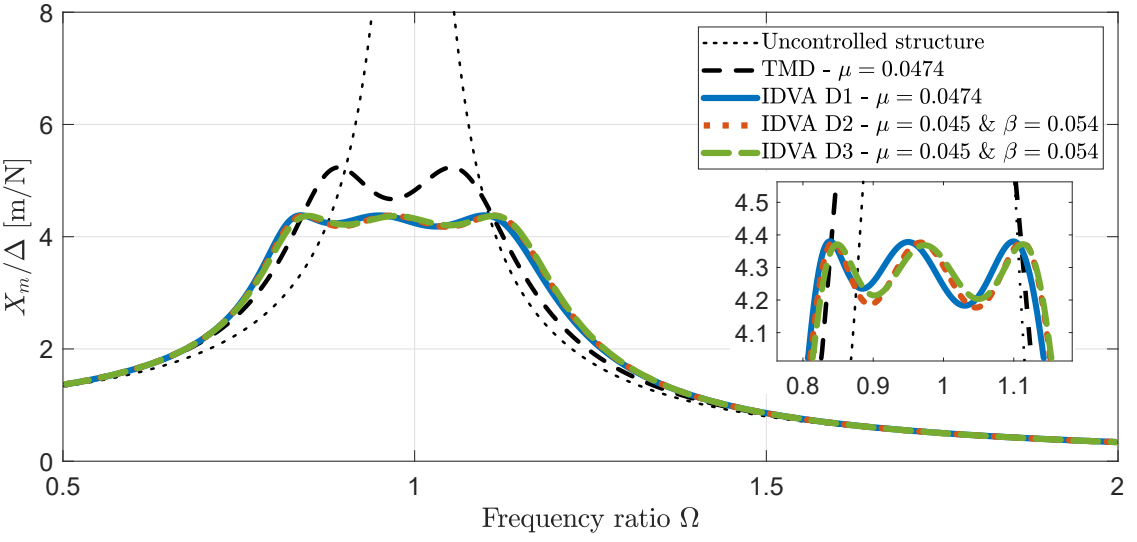


**Figure 2**: Performance comparison of D1, D2, D3, TMD and uncontrolled structure using the optimal dimensionless design parameters given in Table 1. The mass ratio ($\mu$) of TMD and D1, where no parasitic mass exists ($\beta = 0$), considers not only the inertial effect of the auxiliary mass but also the parasitic mass in D2 and D3 for an equitable comparison.

performance and are also very close to the D1 response. All the IDVA designs are visibly better than the TMD performance.

## 3. Design study

The realisation of D1, which is an idealised TID with no parasitic mass, is difficult for applications requiring small inertance because even small amounts of component mass (e.g. the mass of the inerter's terminal or the mass of the terminal of the spring or damper) act as a parasitic mass. In this case, the parasitic mass has a strong effect on the vibration suppression performance and it therefore has to be considered in the mathematical model. Furthermore, in the present study, the practical implementation of the spring-damper arrangement will be accomplished using a complex stiffness mechanism. As a result, the IDVA design is modified from the theoretical concept in D1 to the implementation model in D3 that includes the parasitic mass and the complex stiffness mechanism as shown in Figures 1(a-c).

A pivoted-bar mechanism with flexural-hinges is employed for the inerter design while a simple notch type linear spring is used for the outer spring. Analyses of the fatigue strength and the stiffness at the pivot become important with the use of flexural-hinges. The next subsections present the design methodology, considering the fatigue life-cycle, effect of the stiffness of the flexural-hinges, and the realisation of the damping in the structure.

### 3.1. Inerter design

The force, $F$, produced by an (idealised) inerter is typically modelled using

$$F = b(\ddot{x}_2 - \ddot{x}_1) \tag{12}$$

where $b$ is the inertance with units of kg and $(\ddot{x}_1 - \ddot{x}_2)$ is the relative acceleration of the inerter. The subscripts 1 & 2 refer to the inerter device terminals, and an overdot represents differentiation with respect to time, $t$. Before the introduction of the inerter concept by Smith [1], Flannelly [48] patented the Dynamic Vibration Isolator (DAVI) with a lever mechanism, as shown schematically in Figure 3 (a). This DAVI system is a type of inerter but because of the asymmetry cannot be effectively modelled using Equation 12. John and Wagg [41] developed a pivoted-flywheel inerter device (Figure 3 (b)) which eliminates the asymmetry and therefore can be modelled as a pure inerter term (i.e. a factor of $(\ddot{x}_1 - \ddot{x}_2)$) as in Equation 12 (see also the discussion in [2]). Following a similar approach to [41], the pivoted-bar inerter design proposed in this paper, is shown in Figure 3 (c). This also eliminates the asymmetry relating to the relative acceleration terms in the DAVI system and can therefore be modelled as a pure inerter term, which is proportional to the difference of the accelerations of the terminals. However, there are some important details relating to this, which are explained in the next Subsection.

#### *3.1.1. Mathematical model for the inerter design*

The inerter bar in Figure 3 (c) is subject to both translational and the rotational motion depending on the accelerations of the inerter's terminals. Thus, it can be evaluated as a semi-definite system without considering any connection at the terminals (meaning it is analysed without being connected to ground) [49]. Referring to Figure 3 (c), and neglecting the mass of the legs on the pivots, the kinetic energy of the pivoted-bar inerter can be written as

$$T = \frac{1}{2}m\dot{x}_3^2 + \frac{1}{2}m\dot{x}_2^2 + \frac{1}{2}I\dot{\theta}^2 + \frac{1}{2}m_{bar}\dot{x}_1^2 \tag{13}$$

where $I$ is the rotational moment of inertia of the inerter bar. Assuming the small angle approximation in the inerter bar, linear relationships can be used to define $x_3$ and $\theta$ in terms of $x_1$ (which for this device is the displacement of the centre of the mass of the inerter bar) and $x_2$ (displacement of the lower pivot) as

$$x_3 = 2x_1 - x_2 \;\text{ and }\; \theta = \frac{x_1 - x_2}{l_{bar}/2}. \tag{14}$$

Substituting the first derivative of the expressions in Equation 14 into Equation 13 yields

$$T = \frac{1}{2}m\big(2\dot{x}_1 - \dot{x}_2\big)^2 + \frac{1}{2}m\dot{x}_2^2 + \frac{1}{2}I\Big(\frac{\dot{x}_1 - \dot{x}_2}{l_{bar}/2}\Big)^2 + \frac{1}{2}m_{bar}\dot{x}_1^2. \tag{15}$$

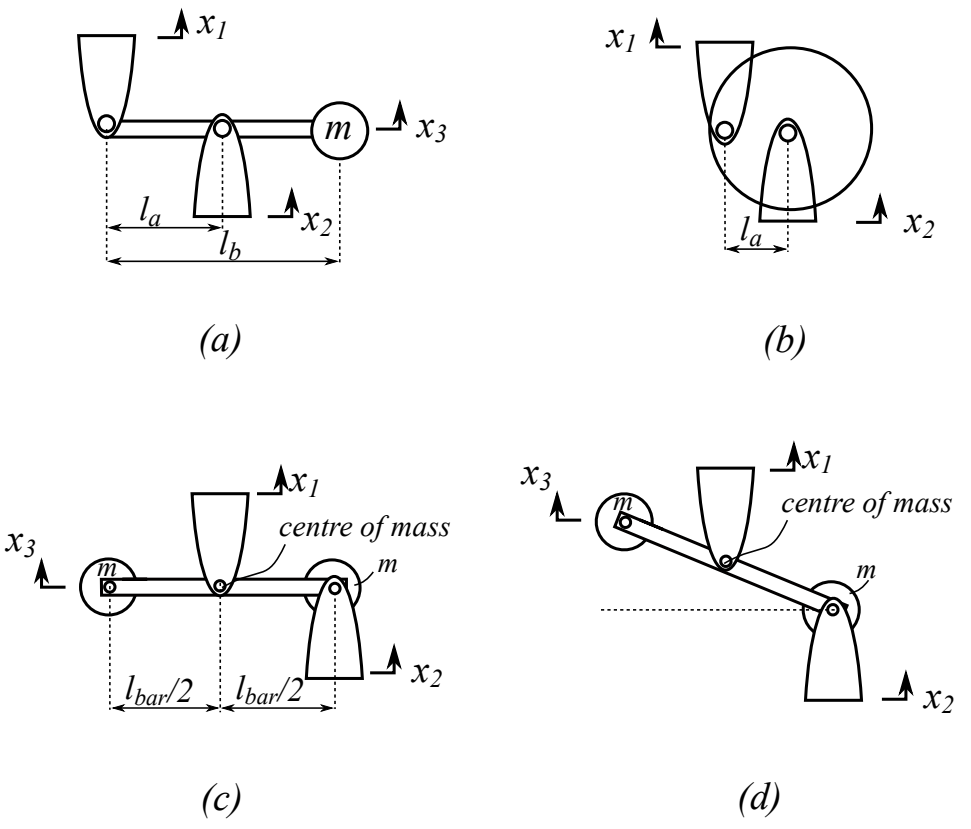


**Figure 3**: Schematic views of (a) the DAVI of Flannelly [48], (b) the pivoted-flywheel inerter device proposed by John and Wagg [41], and (c) the pivoted-bar inerter design proposed in this paper. Relative motion between two terminals of (c) causes a rotation of $\theta$ in the bar as shown in (d).

There is no potential energy, $V$, in the pivoted-bar system as it consists of only inertial elements. Therefore, Lagrange's equation for the system in Figure 3 (c) is written as

$$\frac{d}{dt}\frac{\partial T}{\partial \dot{q}_n} - \frac{\partial T}{\partial q_n} + \frac{\partial V}{\partial q_n} = Q_n \tag{16}$$

where $V = 0$ and $Q_n = 0$ as there are no dissipative or external forces considered. Here $n$ is the number of degrees of freedom and $q_n$ defines the generalised coordinates. The system depicted in Figure 3 (c) has two degrees of freedom being described by $x_1$ and $x_2$. Therefore, two equations of motion are found with respect to $x_1$ and $x_2$. Substituting them into $q_n$ in Equation 16 gives:

$$\text{With respect to } x_1\text{:} \quad (\frac{m_{bar}}{3} + 2m)(\ddot{x}_1 - \ddot{x}_2) + (m_{bar} + 2m)\ddot{x}_1 = 0 \tag{17a}$$

$$\text{With respect to } x_2\text{:} \quad (\frac{m_{bar}}{3} + 2m)(\ddot{x}_2 - \ddot{x}_1) = 0 \tag{17b}$$

where $m_{bar}+2m$ is the mass of the pivoted-bar (i.e. the inerter). Notice that using this analysis, Equation 17a, considers motion with respect to $x_1$ that includes the rigid body motion of the mass of the inerter (which is only proportional to $\ddot{x}_1$) and the relative inertance term. Whereas, Equation 17b, considers motion with respect to $x_2$, but includes only the relative inertance term. The relative inertance coefficient term will be defined to be

$$b = (\frac{m_{bar}}{3} + 2m). \tag{18}$$

Note that $b$ is smaller than the total mass of the pivoted-bar ($m_{bar} + 2m$), and so the total mass of the bar (i.e. inerter) cannot be neglected as it often is in other applications.

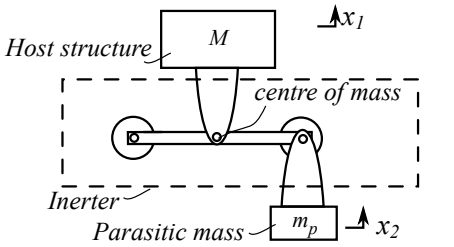


$$b(\ddot{x}_1 - \ddot{x}_2) + (M + m_{bar} + 2m)\ddot{x}_1 = 0$$
$$b(\ddot{x}_2 - \ddot{x}_1) + m_p\ddot{x}_2 = 0$$

*(a)*

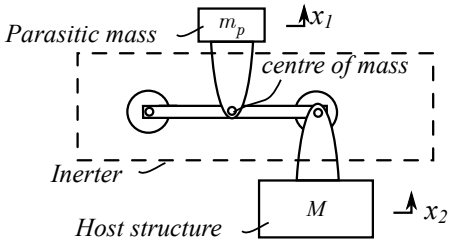


$$b(\ddot{x}_1 - \ddot{x}_2) + (m_p + m_{bar} + 2m)\ddot{x}_1 = 0$$
$$b(\ddot{x}_2 - \ddot{x}_1) + M\ddot{x}_2 = 0$$

*(b)*

**Figure 4**: The inerter is connected to the host structure from the pivot at the centre of mass in (a) and thus, the structural mass of the inerter can be neglected as $m_{bar} + 2m$ can be included with the main mass $M$. In the other case (b), the structural mass of the inerter contributes to the parasitic mass.

| Density, $\rho$ (kg/m$^3$) | Cross section (m x m) | $l_{bar}$ (m) | $m_{bar}$ (kg) |
|---|---|---|---|
| 2700 | 0.015 x 0.015 | 0.080 | 0.0486 |

**Table 2**
Design properties of the inerter device.

Another important factor for this type of design is the attachment configuration, as shown in Figure 4. Here it can be seen that if the pivot in the centre of the bar is connected to the host structure of the system, then the mass of the pivoted-bar acts with the main mass, $M$. In this way, the mass of the pivoted-bar can be excluded from the parasitic mass, Figure 4 (a). In this scenario, it is often the case that $M \gg m_{bar} + 2m$ and so there is little change to the system behaviour. However, if the other pivot is connected to the host structure, the mass of the inerter increases the parasitic mass in the system as shown in Figure 4 (b). This scenario is to be avoided, because it increases the influence of the parasitic mass and this can degrade the system performance slightly, as shown in Figure 2 (dashed red line). Also, in this scenario, adjusting the inertance by adding mass to the inerter bar ($m$) causes an increase in the parasitic mass, which leads to the detuning effect. Each adjustment in the inertance requires a new optimisation to obtain the best design parameters due to change in the parasitic mass.

### *3.1.2. Design and test of the inerter*

Equation 18 gives the inertance value which is used to design the experimental inerter device. The inertance value can be increased by altering the parameters of the pivoted-bar. Figures 5 (a-c) show the schematic views of the realisation of the mechanical model presented in Figure 3 (c). It is possible to adjust the inertance via the addition of two equal masses at both ends of the bar as shown in Figure 5 (c). The mass of the bar, $m_{bar}$ is the main design parameter of the inerter while the masses at each end, $m$, in Equation 18 are used as a fine-tuning adjustment parameter for the inerter. The design properties of the final inerter design are given in Table 2. The pivoted-bar inertance is calculated as 0.0162 kg for the case when the fine-tuning adjustment masses are set to zero.

Figure 5 (d) illustrates the actual inerter device after its manufacture. The pivots were designed as flexure notches to eliminate the friction and maintain a low stiffness. Both flexure notches and the inerter bar were manufactured from

Aluminium material (more details of the design are given in Subsection 3.1.3).

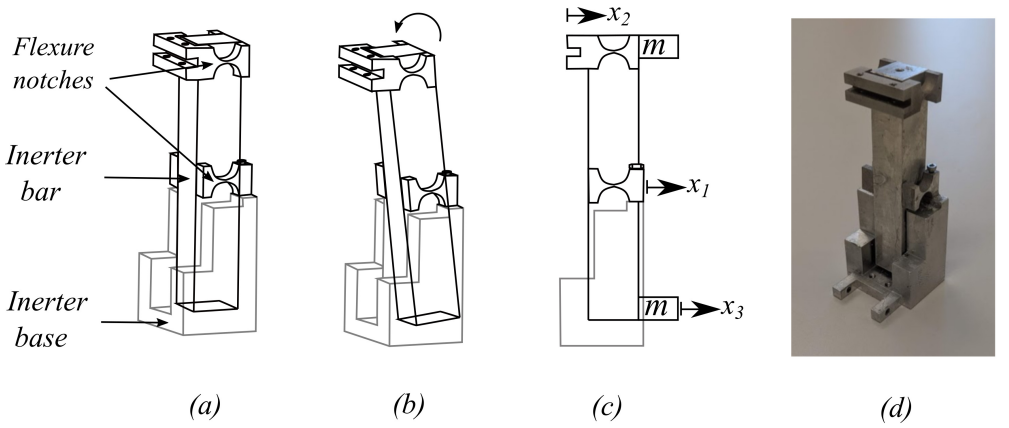


**Figure 5**: Design of the inerter device with flexure notch hinges. The schematic views show (a) equilibrium position, (b) while rotating, and (c) shows the side view with the adjustment masses at both ends of the inerter bar. Plot (d) shows a photograph of the manufactured inerter.

The inerter design in Figure 5 (d) was experimentally tested to evaluate the performance. It was fixed at the base and forced from the upper flexure notch using an impulse hammer. The data was measured from the same point using an accelerometer type PCB 3553B18. The experiments were conducted for a selection of different fine-tuning mass values, and the results are shown in Figure 6 with the theoretical model shown as dashed horizontal lines. The experimentally computed inertance values are computed by taking the inverse of the accelerance response of the device as $b = F/\ddot{x}$ (averaged) for frequencies above 80 Hz. The results show that the inerter device achieves the targeted inertance value (albeit with small fluctuations) for each mass added.

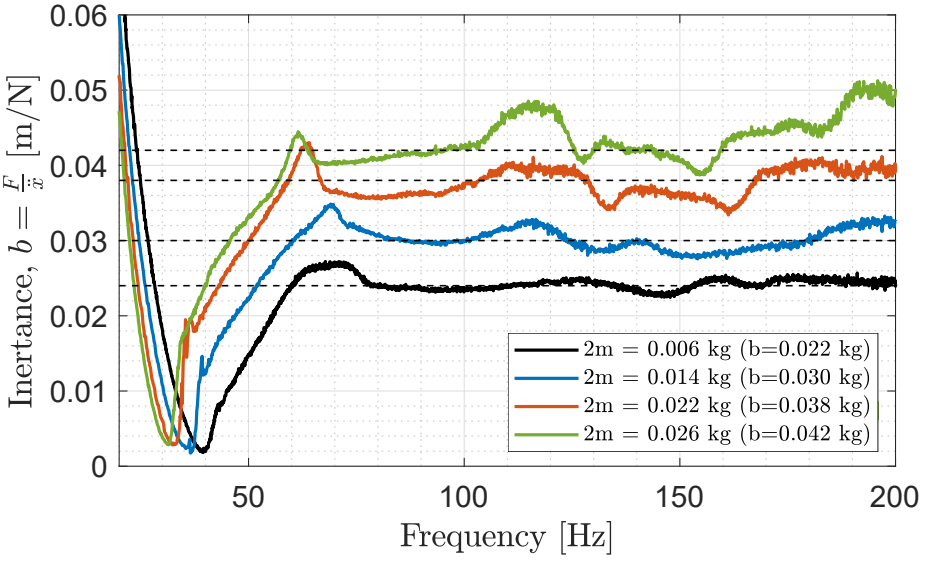


**Figure 6**: Experimental inertance of the pivoted-bar inerter device with the lower flexure fixed and the upper flexure excited with an impact hammer (Dytran 5800B2). 2m in the legend represents the total masses added at both ends (m+m). Dashed horizontal lines indicate the designed inertance value for each case.

| $E$ (GPa) | $w$ (mm) | $t$ (mm) | $R$ (mm) | $l_{bar}$ (mm) | $k_\theta$ (Nm/rad) | $k_{notch}$ (N/m) |
|---|---|---|---|---|---|---|
| 70 | 5 | 0.5 | 4.75 | 80 | 2.0081 | 5020.3 |

**Table 3**
Design parameters of the manufactured semi-circular flexure notches and the theoretical estimation of the total stiffness, where $k_\theta$ is the rotational stiffness of one flexural-hinge and $k_{notch}$ is the total stiffness of four flexural-hinges in Figure 5

### *3.1.3. Design of the flexural-hinges*

Although the use of the flexural-hinges provides the elimination of friction, the stiffness of the flexure notches may still hinder the device from working effectively as an inerter across the required frequency range. Therefore, the resonance region of the inerter device consisting of the pivoted-bar and flexural-hinges should be designed to be as far away from the working frequencies as possible, or the device would have to be modelled as a series-connected inerter-spring arrangement.

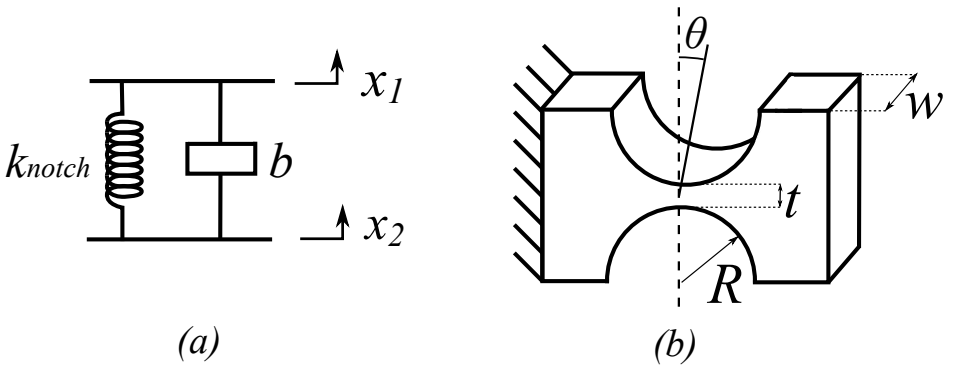


**Figure 7**: (a) Mechanical model of an inerter design with flexural-hinges (b) the illustration of a semi-circular flexure notch.

The mechanical model of the pivoted-bar plus flexural-hinges inerter device can be represented as as idealised inerter and a spring arranged in parallel, as shown in Figure 7 (a). The rotational stiffness for a semi-circular notch hinge, such as that shown schematically in Figure 7 (b), can be estimated as [50]

$$k_\theta \approx \frac{2Ewt^{5/2}}{9\pi R^{1/2}} \tag{19}$$

where $E$, $w$, $t$ and $R$ are Young's Modulus of the material, depth of the flexure notch, thickness of the flexure notch and radius of the flexure notch respectively. The total translational stiffness $k_{notch}$ for the four notches manufactured is presented in Table 3. This was found to be 5020.3 N/m for Aluminium material and $l_{bar} = 80$ mm.

The relative accelerance of the device in Figure 7 (a) is written as

$$\frac{(\ddot{x}_2 - \ddot{x}_1)}{F} = \frac{-\omega^2}{k_{notch} - b\omega^2}, \tag{20}$$

where $F$ is the force generated by the spring-inerter arrangement, $\omega$ is the forcing frequency. The inertance is found by taking the inverse of the accelerance. The effect of the stiffness of the notched on the inertance is shown in Figure 8 for the given values of $E, w, R$ and $l_{bar}$ in Table 3, and consequently, $b = 0.03\ kg$ in Equation 20. The results are also shown for three different values of the notch thickness.

The designed inerter works effectively at frequencies larger than 50 Hz for the notch thickness of 0.1 mm, where an almost constant inertance value can be obtained (dashed black line in Figure 8). However, due to manufacturing limitations, flexural-hinges with a notch thickness of 0.5 mm were manufactured in this study. Therefore, there is a difference between the inertance that is generated by the inerter device with a notch thickness of 0.5 mm and the nominal (or targeted) inertance in the $100 - 200$ Hz frequency band. If required, this difference arising from the stiffness of the flexural hinges can be compensated for by adjusting the inertance, and a similar performance to the

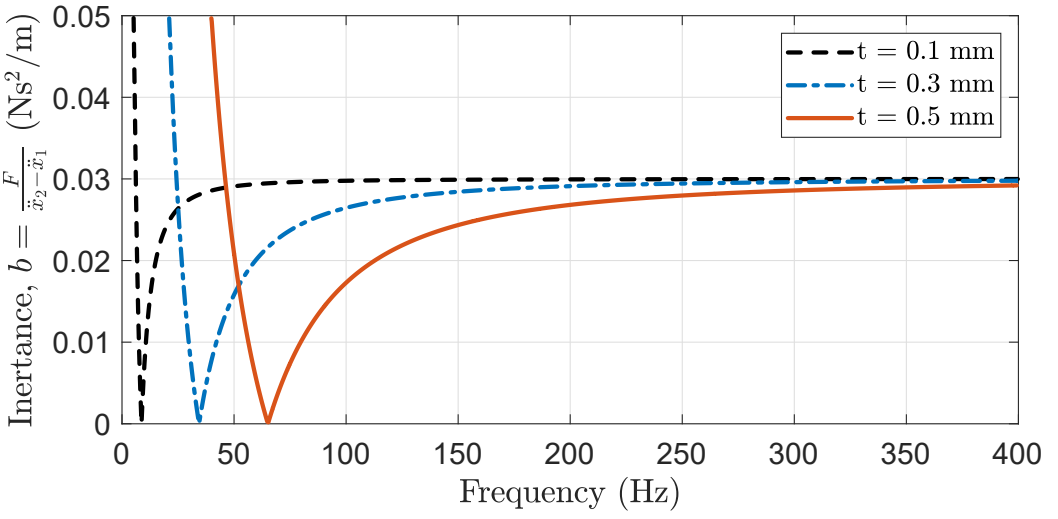


**Figure 8**: Effect of total stiffness of the four flexure notches at the pivots of the bar on the inertance of the inerter (with nominal inertance of 0.03 $kg$) for the notch thicknesses of 0.1 mm, 0.3 mm and 0.5 mm.

pure inerter ($k_{notch} = 0$) can be achieved — as presented in Section 4. It should be noted that the flexure stiffness of the experimental result presented in Figure 6 is half of the total since one of the terminals where the measurement happened was free.

The effective working frequency band of the pivoted-bar inerter is defined by the resonance region of the system in Figure 7a. For low effective working frequency band, the resonance region must be shifted to as lower frequencies as possible. This can be achieved by having either smaller notch stiffness or higher inertance in the denominator of Equation 20. For a given inertance, the notch stiffness can be reduced by changing the geometric properties or material from Equation 19. For instance, reducing the notch thickness $t$ reduces the notch stiffness and shifts the resonance region to lower frequencies. Further reduction in the stiffness can be provided by choosing a material with lower Young's modulus. For high frequency applications, it is important to consider the fatigue life-cycle of the flexural hinge and choose a material with a reasonable fatigue strength. For low frequency applications, the focus on the material choice can be Young's modulus as fatigue life-cycle ceases to be one of the main issues.

One of the main issues in the use of the flexural mechanism such as the notch hinges is fatigue failure. The life-cycle of the absorber under harmonic excitation can be significantly reduced due to the fatigue failure of the notch hinges. The fatigue life of the flexural-hinges can be improved by smaller notch thickness as the maximum stress, which occurs in the thinnest section of the notch, decreases with decreasing notch thickness. Hence, the allowable rotational stroke of the pivoted-bar without the fatigue failure is increased. The fatigue life-cycle analysis of the flexural-hinges is presented in Appendix B.

## 3.2. Design and test of the damper

In the present study, a silicone gel material was chosen for the damping component. This material was relatively straightforward to manufacture and incorporate into a small size device [51]. Hysteretic damping with complex stiffness is used to model the gel, assuming that the mechanical properties of the gel are frequency-independent. The application of linear hysteretic damping into both the TID and TMDI was previously studied by Deastra et al. [42].

The silicone gel used in the experiments was based on polyorganosiloxanes (named Magic Power Gel, from Raytech) and consists of a mixture of two components and the mixing ratio defines the loss factor and Young's modulus. Previous studies have shown that the damping (loss factor) and elastic (Young's Modulus) properties of the silicon gel remain unchanged under different temperature and different dynamic strain at room temperature [52, 53, 54]. The silicone gel with a mixing ratio of 1:1.1 was used to create the sliding plate device shown in Figure 9 (a). The gel on both sides works on the shear plane and thus, noting that the shear modulus equals $G = \frac{E}{2(1+\nu)}$, the stiffness of the gel

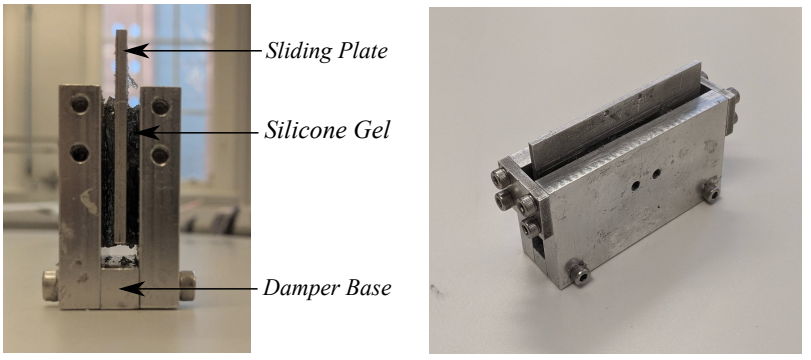


**Figure 9**: Gel damper consisting of a sliding plate and two silicone gel layers: (a) side view and (b) isometric view of the manufactured gel damper.

| | Total mass, $m$ (gram) | Nat. freq., $\omega_n$ (Hz) | Loss factor, $\eta$ | Stiffness, $k_i$ kN/m |
|---|---|---|---|---|
| Test a (Figure 10a) | 38.5 | 110 | 0.545 | 23.4 |
| Test b (Figure 10b) | 49.5 | 130 | 0.515 | 26.3 |
| Test c (Figure 10c) | 66.5 | 141 | 0.505 | 25.3 |
| Average | – | – | 0.5217 | 24.97 |

**Table 4**
Loss factor and the stiffness of the gel obtained from three tests with their average values.

damper can be calculated as:

$$k_i = \frac{EA}{(1+\nu)d} \tag{21}$$

where $E$ is Young's modulus corresponding to 1:1.1 mixing ratio, $A$ is the area of the gel, $d$ is the thickness of the gel and $\nu$ is the Poisson's ratio, which is assumed to be 0.5 [54]. Equation 21 shows that the stiffness of the gel damper can be adjusted by setting the area and the thickness of the gel. A gel damper with two identical gel layers with an area of 35 mm x 45 mm and a thickness of 3 mm on both side was manufactured as shown in Figure 9 (b).

In order to measure and evaluate the frequency-dependency of the mechanical properties of the gel under the working frequencies, the impulse hammer test was applied to the gel damper. It was fixed from the damper base and a small aluminium block was added to the sliding part for the connection of the accelerometer. The natural frequency of the gel damper was increased by adding mass since the effects of the loss factor and the stiffness of the gel becomes more apparent around resonance. Three cases were conducted: no additional mass added, the total mass was increased by 11 gram and 28 gram. The impulse hammer was applied by hitting the small aluminium block. The accelerance of the gel damper is written as:

$$\frac{\ddot{x}}{F} = \frac{-\omega^2}{k_i(1+j\eta) - m\omega^2} \tag{22}$$

where $k_i$ and $\eta$ are the stiffness and the loss factor of the gel, $\omega$ is the forcing frequency and $m$ is the total mass of the sliding plate, aluminium block and the accelerometer, which is 38.5 gram. The loss factor and the stiffness of the gel were found by fitting $k_i$ and $\eta$ in Equation 22 to the experimental curve for known mass values.

The mechanical properties of the gel fitted are given in Table 4. The experimental results in comparison with the numerical simulation using the corresponding mechanical properties are presented in Figure 10 (a-c), respectively. They are also compared with the average values of the loss factors and the stiffness obtained from three cases.

It was observed that there is no significant change in the stiffness and the loss factor of the gel between 100 Hz and 150 Hz, which are the working frequency of the absorber. The required loss factor $\eta$ of 0.5217 and stiffness $k_i$ of 24.97 $kN/m$ were achieved.

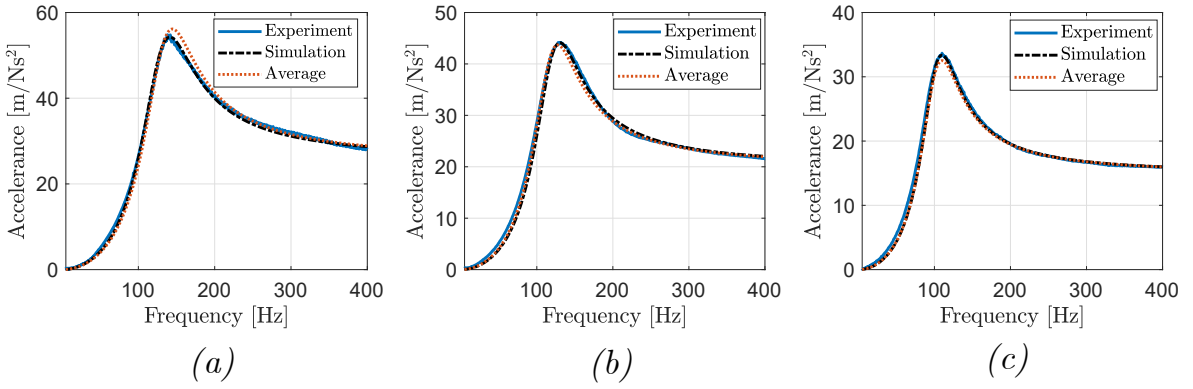


**Figure 10**: Experimental results of the modal tests of the gel damper applied with a impulse hammer in comparison with numerical simulations obtained by Equation 22 and the average values of the three cases: (a) no mass added, (b) 11 gram mass and (c) 28 gram mass added.

## 3.3. Final design

The inerter-based dynamic vibration absorber (D3) after final assembly is shown in Figure 11. In the design D3 in Figure 1(c), a series connection of a hysteretic spring/damper $k_i(1 + j\eta)$, a parasitic mass $m_p$ and an inerter $b$ is connected in parallel to an outer spring $k_o$. An auxiliary mass is added to the hysteretic spring/damper side, and the whole system is attached to the host structure from the inerter side. In Figure 11, the gel damper operates as the hysteretic spring/damper. The sliding plate acts as the parasitic mass and provides the series connection between the gel damper and the inerter. The gel damper's base (the damper-inner spring's base) is also the auxiliary mass. The prototype realises the design D3 as the series connection of the gel damper, the sliding plate and the inerter is parallel connected to the outer spring between the auxiliary mass and the host structure after the attachment of the prototype to the host structure from the absorber base.

The prototype includes a notch type linear spring as the outer spring ($k_o$ in Figure 1 (c)) with a stiffness of 251.89 kN/m. The mass of the damper-inner spring base is accounted for as part of the auxiliary mass since it is completely supported by the outer spring. The total auxiliary mass and consequently, the mass ratio is set by mounting additional mass on the damper-inner spring base shown in Figure 11.

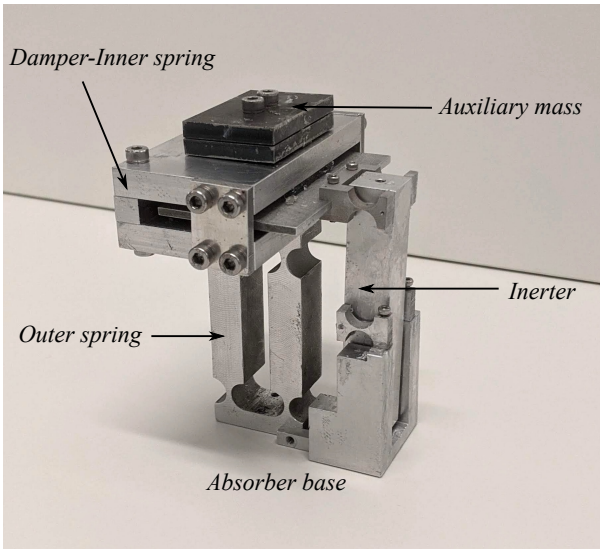


**Figure 11**: The prototype manufactured after the assembly.

The mass of the sliding plate, as shown in Figure 9, is an isolated mass that cannot be included as part of the auxiliary mass nor the host structure and acts as a parasitic mass of 0.026 kg in the system. Although it can be reduced, it would be difficult to completely avoid the parasitic mass effect due to small inertance values as previously discussed.

# 4. Experimental testing

## 4.1. Experimental setup and dynamic properties

The experimental setup to test the prototype is presented in Figure 12. An aluminium block that is fixed to a compliant mechanism is used for the host structure so that the dominant mode of the host structure is in the horizontal direction. The prototype is placed to the top surface of the aluminium block attached at the base. Modal tests of the structure with and without the prototype were conducted with the impulse hammer Dytran 5800B2 and the accelerometer PCB 353B18. The impulse hammer was applied to the aluminium block in the direction of the dominant mode and the acceleration was measured from the same direction. The data were acquired and processed with LMS Test.Lab. The dominant vibration mode in the horizontal direction of the host structure was measured at 117.3 Hz with the modal mass of 10.7 kg and damping of 2.3%.

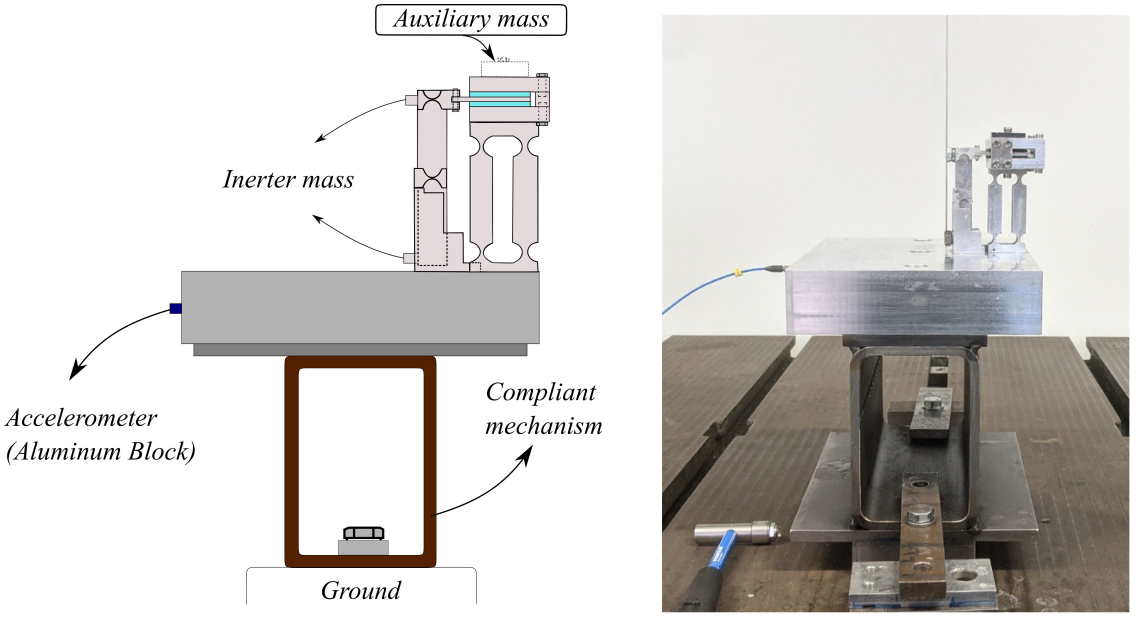


**Figure 12**: Experimental setup where the prototype is tested on an Aluminium block (host structure mass) attached to a compliant mechanism (host structure stiffness).

## 4.2. Tuning parameters for experiment

Based on the dynamic properties of the host structure, the optimal design parameters for D3 were obtained from the dimensionless design parameters (as given in Table 1) for $\mu = 0.045$ and $\beta = 0.054$, considering a parasitic mass of 0.026 kg due to the mass of the sliding plate between the gel layers. Initially, design parameters were obtained assuming a constant inertance value at each frequency. However, for the notch thickness of 0.5 mm, the inerter does not provide a constant inertance at the effective working frequency band of this experimental case due to the stiffness of the flexure notches as discussed in Section 3.1.3. Hence, an equivalent optimal inertance was also obtained by considering the spring-inerter arrangement (as shown in Figure 7 (a)) instead of just an inerter element. The notch stiffness was determined as 5020.3 N/m from the theoretical estimation. However, it was estimated that the actual stiffness value is around 9000 N/m on the flexure notches due to possible stress stiffening (owing to assembly and the load of mass added to the inerter bar) and manufacturing errors.

Constraining all design parameters except the inertance to their optimal design values, the equivalent optimal inertance values was found using a SaDE numerical optimisation. The optimal design parameters for the constant

| | $k_o$ (kN/m) | $k_i$ (kN/m) | $\eta$ | $b$ (kg) | $H_{max}$ (m/N) |
|---|---|---|---|---|---|
| D3 ($k_{notch} = 0$) | 254.51 | 24.84 | 0.5114 | 0.032 | 7.52 x $10^{-7}$ |
| D3 ($k_{notch} = 5020.3$ N/m) | 254.51* | 24.84* | 0.5114* | 0.043 | 7.69 x $10^{-7}$ |
| D3 ($k_{notch} = 9000$ N/m) | 254.51* | 24.84* | 0.5114* | 0.052 | 7.86 x $10^{-7}$ |

*constrained parameters

**Table 5**
Optimal design parameters obtained by performing SaDE for numerical optimisation for the notch stiffness of 0, 5020.3 N/m and 9000 N/m. $H_{max}$ corresponds to the maximum amplitude in the FRF obtained from numerical optimisation.

inertance case and the variable inertance cases where the notch stiffness is taken into account are given in Table 5. The actual values of the experimental parameters were also identified. In this case, the actual stiffness of the outer spring $k_o$ was measured as 251.89 kN/m, the stiffness $k_i$ and the loss factor $\eta$ were found to be 24.97 kN/m and 0.5217 respectively, which is the same as stated in Section 3.2.

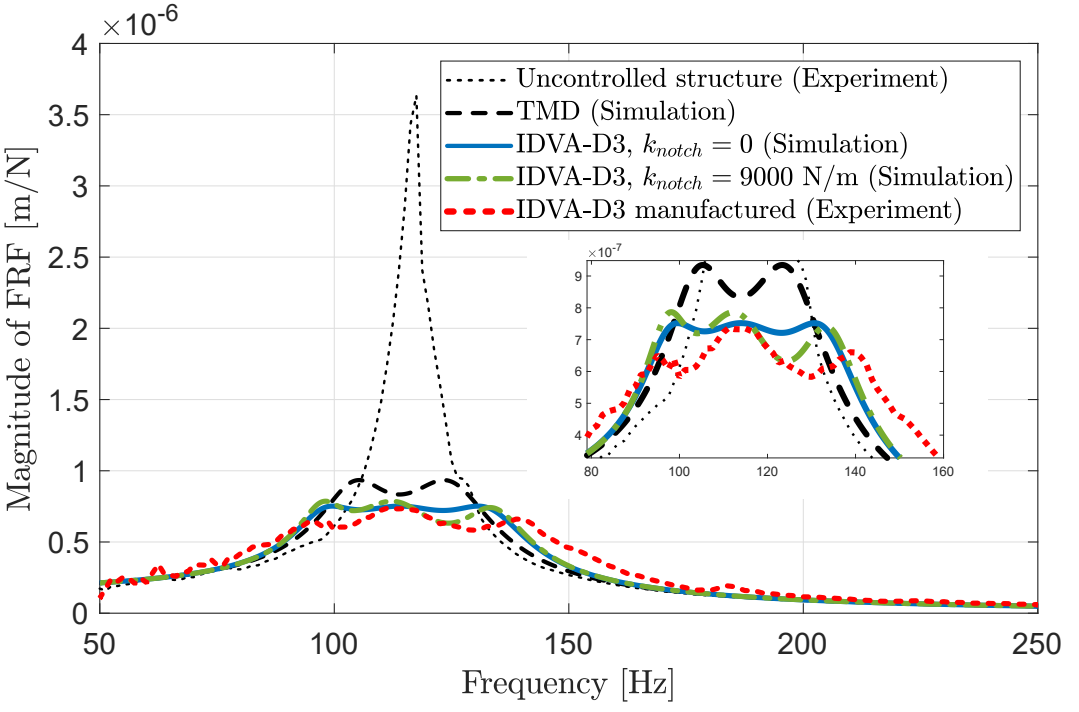


**Figure 13**: Experimental results of the host structure with the prototype (IDVA-D3 manufactured) with a mass ratio of 0.045 and a parasitic mass ratio of 0.054 in comparison with the experimental result of the uncontrolled host structure, and the numerical simulations of D3 (for $k_{notch} = 0$ and $k_{notch} = 9000$ N/m) with the design parameters presented in Table 5 and a classical TMD.

## 4.3. Experimental results

The magnitude of the frequency response function (FRF) of the host structure obtained from the modal tests with the impulse hammer is shown in Figure 13. Here the FRF of the host structure without the prototype is shown as the "uncontrolled structure" (black dotted line) compared with the host structure with the prototype which is "IDVA-D3 manufactured" (red dotted line). As would be expected, the addition of the prototype leads to a large reduction in the resonant response of the host structure.

Also numerical simulations of a TMD (black dashed line) and two cases of D3 (blue solid and green dashed lines) are plotted for comparison in Figure 13. The numerical simulation for the TMD was obtained from optimal design parameters (as given in Table 1) for $\mu_{D3}(1 + \beta_{D3}) = 0.0474$, taking the effect of the parasitic mass into account in

the comparison. The numerical simulation results for D3 were obtained using the optimal design parameters given in Table 5 for $\mu = 0.045$ and $\beta = 0.054$, and two case are shown for $k_{notch} = 0$ (blue) and $k_{notch} = 9000$ (green).

The prototype reduced the maximum amplitude of the host structure from 36.34 x $10^{-7}$ m/N to 7.37 x $10^{-7}$ m/N, which corresponds to 79.7% vibration suppression as seen in Figure 13. This means that the prototype has shown 18.1% performance improvement than a classical TMD when it compared with the numerical simulation result of the host structure with TMD.

Simulation results demonstrate that the stiffness of the flexure notch of 9000 N/m increases the maximum amplitude by 4.5% compared to zero notch stiffness (pure inerter) when the inertance is properly adjusted. This shows that the IDVA design with the notch stiffness can still effectively suppress the vibration in practice. It is worth pointing out that the 4.5% increase in the maximum amplitude due the notch stiffness can be decreased to smaller than 1% if the constraints are removed on the design parameters (marked with an asterisk in Table 5) in the optimisation. The experimental case studied in this paper shows that adjustable inertance was helpful for fine tuning. Furthermore, the effect of notch stiffness can be compensated for using the adjustable inertance, leading to a performance very similar to the idealised case with zero hinge stiffness.

The result shows that the prototype effectively suppressed the vibration without a grounded connection. In order to further demonstrate the effectiveness of the prototype proposed in this paper, experimental FRFs of the host structure with the prototype for different inertance and auxiliary mass values are presented in Figure 14. Three auxiliary mass values of 0.365 kg, 0.480 kg and 0.530 kg, and four inertance values of 0.020 kg, 0.030 kg, 0.043 kg and 0.054 were tested. Numerical simulation results in Figure 14 were obtained by using the actual values of the elements of the IDVA ($k_o = 251.89$ kN/m, $k_i = 24.97$ kN/m and $\eta = 0.5217$), which are close to the optimal design parameters presented in Table 5.

Figure 14 demonstrates that the prototype responds to the change in the inertance for different auxiliary masses. The experimental results presented in Figure 14 have a very close agreement with the simulation results. The deviations between the experimental results and the numerical simulations and the design remarks will be discussed in the next section.

## 5. Discussion

The experimental results have shown that D3 can effectively suppress the vibrations and obtain an improved performance when compared to a classical TMD. One of the important properties of the design is that the inertance can be adjustable by simply adding masses to both ends of inerter bar. This provides a method for fine tuning the inertance during or after device manufacture, that can be used to reduce the detuning effects caused by the other components. For example, as shown in Figure 13, comparable vibration suppression performances have been obtained for the cases where the notch stiffness is neglected ($k_{notch} = 0$) and included ($k_{notch} = 9000$) by just increasing the inertance values from 0.032 kg to 0.052 kg as shown in Table 5.

It can be noted that although the average inertance can be successfully increased to the desired value by adding masses, this also increases the fluctuations in inertance values as shown in Figure 6. Adding excessive amounts of mass could also shift the higher modes into the working frequency range of the absorber. Hence, it is suggested that the added mass should only be used for relatively small adjustments of the inertance after the appropriate choice of $m_{bar}$ in Equation 18. The experimental results presented in Figure 14 have deviations from the numerical results obtained for $k_{notch} = 9000$ N/m for smaller inertance values (0.020 kg and 0.030 kg). For these values, better results are observed when the theoretical stiffness $k_{notch} = 5020.3$ N/m is considered in the numerical simulations. A possible explanation is that adding mass to the inerter bar increases the stiffness due to a stress stiffening effect in the flexure hinges.

One of the important points that shortens the operation life of mechanical device involving compliant mechanisms such as flexure notch is the fatigue life-cycle. Although the fatigue life of the flexural-hinges was not experimentally tested, the importance of the fatigue analysis should be highlighted for high frequency applications. It has been observed that smaller notch thickness helps the increase the fatigue life in addition to reducing the notch stiffness. In this study the notch thickness was limited by manufacturing constraints.

The novelty of the practical design proposed is that it does not require direct attachment to inertial ground or deployment between two adjacent storeys when compared with the idealised IDVA in [14]. It can be connected to a host structure without a grounded element, which in practice is similar to the classical use of a TMD. The design is applicable for small-size applications. It can be also employed for inertial grounded inerter applications such as TMDIs [10] or non-traditional inerter-based dynamic vibration absorbers [16, 17] with small adjustments.

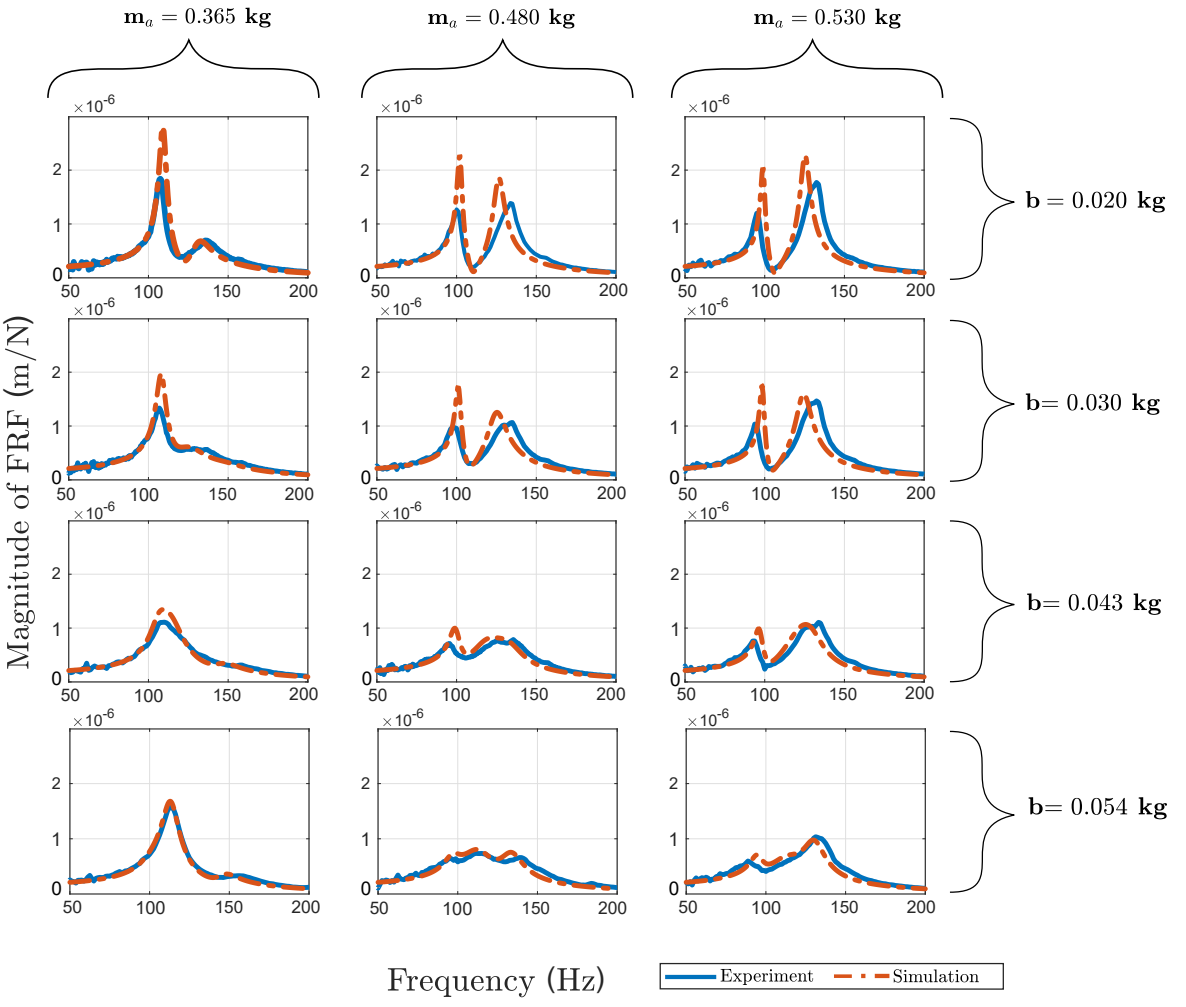


**Figure 14**: Experimental FRFs of the D3 with the notch stiffness of 9000 N/m for auxiliary mass of 0.365 kg, 0.480 kg and 0.530 kg (each column corresponds a constant mass) and inertance of 0.020 kg, 0.030 kg, 0.043 kg and 0.054 kg (each row corresponds a constant mass) in comparison with the numerical simulations.

## 6. Conclusions

This paper has presented a new design for an inerter-based dynamic vibration absorber which is applicable to restricted-space applications without the need for an inertial ground. It allows straightforward implementation and deployment in a similar way to the classical tuned mass damper (TMD). The pivoted-bar mechanism is designed to act as a pure inerter, and avoids unbalanced inertance effects such as those that occur in the dynamic antiresonant vibration isolator (DAVI). The effects of parasitic mass have been minimised by using (i) the appropriate device arrangements, (ii) numerical optimisation, and (iii) fine tuning of the device by adding small additional masses. The optimum device damping values were obtained by using a gel damper that can be modelled as a hysteretic damper. The design uses frictionless flexure hinges that have a small amount of stiffness that can affect the device performance. It was shown how this can also be compensated for using the design optimisation and fine tuning strategies.

The design was experimentally tested with a damped single degree-of-freedom host structure and an 18% vibration improvement was obtained compared to a classical TMD.

The main contribution of the present study is that a new design for the IDVA which is physically employable for small-scale applications has been proposed. The design does not require direct attachment to an inertial ground or deployment between two different parts of the structure. It provides a more versatile solution by being directly attached to the host structure with an auxiliary mass like a classical TMD.

An important aspect of the design is the adjustable inertance. The inertance of the inerter proposed can be relatively simply adjusted by adding fine tuning masses. This provides a potentially useful feature to overcome the detuning effects and other uncertainties in the system. The use of flexure notches in the pivoted-bar inerter were advantageous for frictionless design compared to traditional inerters (rack and pinion, ball-screw and fluid-base inerters). It was shown how the resulting changes in performance can be accounted for, alongside fatigue issues. An experimental study of the fatigue behaviour of these type of flexure hinges is a topic for future work. The idea of flexure hinges for inerter design extends the initial work of [41], and in this case has provided a straightforward method for realisation of the inerter-spring arrangement. Also, in the vibration suppression case, only $H_\infty$ optimisation problem was considered and random excitation was not analysed. Tuning the prototype for $H_2$ optimisation and its experimental verification remains to be future work.

The new design of the inerter-based absorber has the potential for implementation in applications with restricted-space under forced excitation. As it can be applicable in a similar manner to the classical TMD, this design concept could allow the replacement for a TMD in most applications. For instance, it is employable for chatter suppression of flexible workpieces in milling operations, which generally allows limited spaces for passive control devices or vibration suppression of cantilever-like structures under force excitation where grounded connections of the passive control devices are difficult.

## CRediT authorship contribution statement

**Hakan Dogan:** Investigation, Methodology, Software, Writing - original draft. **Neil D. Sims:** Supervision, Writing - review & editing. **David J. Wagg:** Supervision, Writing - review & editing.

## Declaration of Competing Interest

The authors declare that they have no known competing financial interests or personal relationships that could have appeared to influence the work reported in this paper.

## Acknowledgement

The first author would like to acknowledge the support from the Turkish Ministry of National Education by providing the scholarship.

## Appendix A Dimensionless expression for frequency response functions

Using the dimensionless parameters in Equation 3, the FRFs in Equations 8-10 can be expressed, respectively as

$$|H_{D1}(\Omega,\delta,\gamma,\alpha,\zeta_a,\zeta_m,\mu)| = \sqrt{\frac{H_{num_1,D1}(\Omega,\delta,\gamma,\alpha)+H_{num_2,D1}(\Omega,\delta,\gamma,\zeta_a)}{H_{den_1,D1}(\Omega,\delta,\gamma,\alpha,\zeta_a,\zeta_m,\mu)+H_{den_2,D1}(\Omega,\delta,\gamma,\alpha,\zeta_a,\zeta_m,\mu)}}, \tag{A.1}$$

$$|H_{D2}(\Omega,\delta,\gamma,\alpha,\beta,\zeta_a,\zeta_m,\mu)| = \sqrt{\frac{H_{num_1,D2}(\Omega,\delta,\gamma,\alpha,\beta,\zeta_a)+H_{num_2,D2}(\Omega,\delta,\gamma,\alpha,\beta,\zeta_a)}{H_{den_1,D2}(\Omega,\delta,\gamma,\alpha,\beta,\zeta_a,\zeta_m,\mu)+H_{den_2,D2}(\Omega,\delta,\gamma,\alpha,\beta,\zeta_a,\zeta_m,\mu)}}, \tag{A.2}$$

$$|H_{D3}(\Omega,\delta,\gamma,\alpha,\beta,\eta,\zeta_m,\mu)| = \sqrt{\frac{H_{num_1,D3}(\Omega,\delta,\gamma,\alpha,\beta,\eta)+H_{num_2,D3}(\Omega,\delta,\gamma,\alpha,\beta,\eta)}{H_{den_1,D3}(\Omega,\delta,\gamma,\alpha,\beta,\eta,\zeta_m,\mu)+H_{den_2,D3}(\Omega,\delta,\gamma,\alpha,\beta,\eta,\zeta_m,\mu)}}, \tag{A.3}$$

where the expressions for $H_{num_1}$, $H_{num_2}$, $H_{den_1}$ and $H_{den_2}$ are given as following:

$$H_{num1,D1}(\Omega,\delta,\gamma,\alpha)=\Big[-\delta\Big(-\Omega^4+\gamma^2\big(1+(\delta+1)\alpha^2\big)\Omega^2-\alpha^2\gamma^4\Big)\Big]^2$$

$$H_{num2,D1}(\Omega,\delta,\gamma,\zeta_a)=\Big[-2\zeta_a\gamma\big((\delta+1)\Omega^2-\gamma^2\big)\Omega\Big]^2$$

$$\begin{aligned}H_{den1,D1}(\Omega,\delta,\gamma,\alpha,\zeta_a,\zeta_m,\mu)=\Big[&-\delta\Omega^6+\Big(\alpha^2\gamma^2(\mu+1)\delta^2+\big(1+(\alpha^2+\mu+1)\gamma^2+4\gamma\zeta_a\zeta_m\big)\delta+4\gamma\zeta_a\zeta_m\Big)\Omega^4\\&-\gamma^2\Big(\alpha^2\delta^2+\big(\alpha^2\gamma^2(\mu+1)+\alpha^2+1\big)\delta+4\gamma\zeta_a\zeta_m\Big)\Omega^2+\delta\gamma^4\alpha^2\Big]^2\end{aligned}$$

$$\begin{aligned}H_{den2,D1}(\Omega,\delta,\gamma,\alpha,\zeta_a,\zeta_m,\mu)=\Big[&2\Omega\Big(\Big(\zeta_a\big(1+(\mu+1)\delta\big)\gamma+\zeta_m\delta\Big)\Omega^4-\gamma\Big(\zeta_a(\mu+1)\gamma^2+\delta\zeta_m(\delta\alpha^2+\alpha^2+1)\gamma+\zeta_a(\delta+1)\Big)\Omega^2\\&+\gamma^3(\delta\alpha^2\gamma\zeta_m+\zeta_a)\Big)\Big]^2\end{aligned}$$

$$H_{num1,D2}(\Omega,\delta,\gamma,\alpha,\beta,\zeta_a)=\Big[\gamma\Big(\big((4\beta+4\delta+4)\zeta_a^2+\alpha^2\delta(\beta+\delta)\big)\Omega^4-\gamma^2\big(\delta^2(\beta+\delta+1)\alpha^4+\alpha^2\delta(\beta+\delta)+4\zeta_a^2\big)\Omega^2+\alpha^4\delta^2\gamma^4\Big)\Big]^2$$

$$H_{num2,D2}(\Omega,\delta,\gamma,\alpha,\beta,\zeta_a)=\Big[2\zeta_a\Omega\big((\beta+\delta)\Omega^4-\gamma^2\Omega^2(2\beta\alpha^2\delta+2\alpha^2\delta^2+2\alpha^2\delta+\beta+\delta)\Omega^2+2\alpha^2\delta\gamma^4\big)\Big]^2$$

$$\begin{aligned}H_{den1,D2}(\Omega,\delta,\gamma,\alpha,\beta,\zeta_a,\zeta_m,\mu)=\Big[&-\Big(\Big[\Big(\big((4\beta\mu+4\mu+4)\delta+4\beta+4\big)\zeta_a^2+\alpha^2\delta\big((\beta\mu+1)\delta+\beta\big)\Big)\gamma+4\zeta_a\zeta_m(\beta+\delta)\Big]\Omega^6\\&-\gamma\Big[\Big(\Big(\alpha^4(\beta\mu+\mu+1)\delta^3+\big((\beta+1)\alpha^2+\beta\mu+\mu+1\big)\alpha^2\delta^2+\alpha^2\beta(\mu+1)\delta+4\zeta_a^2(\beta\mu+\mu+1)\Big)\gamma^2\\&+8\zeta_a\zeta_m\Big(\alpha^2\delta^2+\big(\frac{1}{2}+(\beta+1)\alpha^2\big)\delta+\frac{\beta}{2}\Big)\gamma+\alpha^2\delta^2+(\alpha^2\beta+4\zeta_a^2)\delta+4\zeta_a^2(\beta+1)\Big)\Big]\Omega^4\\&+\gamma^3\Big[\delta^2\big(\delta+(\beta\mu+\mu+1)\gamma^2+\beta+1\big)\alpha^4+\delta(8\gamma\zeta_a\zeta_m+\beta+\delta)\alpha^2+4\zeta_a^2\Big]\Omega^2-\alpha^4\delta^2\gamma^5\Big)\Big]^2\end{aligned}$$

$$\begin{aligned}H_{den2,D2}(\Omega,\delta,\gamma,\alpha,\beta,\zeta_a,\zeta_m,\mu)=\Big[&2\Omega\Big(-\zeta_a(\delta\beta\mu+\beta+\delta)\Omega^6+2\Big[2\gamma\zeta_m(\beta+\delta+1)\zeta_a^2+\Big(\Big(\alpha^2(\beta\mu+\mu+1)\delta^2\\&+\big((\alpha^2+\frac{\mu}{2})\beta+\alpha^2+\frac{\mu}{2}+\frac{1}{2}\big)\delta+\frac{\beta(\mu+1)}{2}\Big)\gamma^2+\frac{\beta}{2}+\frac{\delta}{2}\Big)\zeta_a+\frac{\alpha^2\delta\gamma\zeta_m(\beta+\delta)}{2}\Big]\Omega^4\\&-2\gamma^2\Big[\frac{\alpha^4\delta^3\gamma\zeta_m}{2}+\frac{\big(\gamma\zeta_m(\beta+1)\alpha^2+\gamma\zeta_m+2\zeta_a\big)\alpha^2\delta^2}{2}+\Big(\big(\zeta_a(\beta\mu+\mu+1)\gamma^2+\frac{\beta\gamma\zeta_m}{2}\\&+\zeta_a(\beta+1)\big)\alpha^2+\frac{\zeta_a}{2}\Big)\delta+\frac{\zeta_a(4\gamma\zeta_a\zeta_m+\beta)}{2}\Big]\Omega^2+\alpha^4\delta^2\gamma^5\zeta_m+2\alpha^2\delta\gamma^4\zeta_a\Big)\Big]^2\end{aligned}$$

$$H_{num1,D3}(\Omega,\delta,\gamma,\alpha,\beta,\eta) = \left[(\beta+\delta)\Omega^4 + \gamma^2\Big(\alpha^2(\eta^2-1)\delta^2 + \big(-1+(\beta\eta^2+\eta^2-\beta-1)\alpha^2\big)\delta-\beta\Big)\Omega^2 - \alpha^2\delta\eta^2\gamma^4 + \alpha^2\delta\gamma^4\right]^2$$

$$H_{num2,D3}(\Omega,\delta,\gamma,\alpha,\beta,\eta) = \left[\eta\Big(\beta+\delta)\Omega^4 - \gamma^2(2\alpha^2\beta\delta + 2\alpha^2\delta^2 + 2\alpha^2\delta + \beta + \delta)\Omega^2 + 2\alpha^2\delta\gamma^4\Big)\right]^2$$

$$\begin{aligned} H_{den1,D3}(\Omega,\delta,\gamma,\alpha,\beta,\eta,\zeta_m,\mu) = \Bigg[\Bigg( & -(\beta\delta\mu+\beta+\delta)\Omega^6 - 2\eta\zeta_m(\beta+\delta)\Omega^5 - \Big[\Big(\alpha^2(\eta-1)(\eta+1)(\mu\beta+\mu+1)\delta^2 + \big((\beta\eta^2+\eta^2-\beta-1)\alpha^2 \\ & -\mu\beta-\mu-1\big)\delta - \beta(\mu+1)\Big)\gamma^2 - \beta - \delta\Big]\Omega^4 + 2\gamma^2\zeta_m\eta(2\alpha^2\beta\delta + 2\alpha^2\delta^2 + 2\alpha^2\delta + \beta + \delta)\Omega^3 \\ & + \gamma^2\Big[\alpha^2(\eta^2-1)\delta^2 + \Big(-1+(\eta+1)(\eta-1)\big((\mu\beta+\mu+1)\gamma^2+\beta+1\big)\alpha^2\Big)\delta - \beta\Big]\Omega^2 \\ & - 4\alpha^2\delta\eta\gamma^4\zeta_m\Omega - \alpha^2\delta\eta^2\gamma^4 + \alpha^2\delta\gamma^4\Big)\Bigg]^2 \end{aligned}$$

$$\begin{aligned} H_{den2,D3}(\Omega,\delta,\gamma,\alpha,\beta,\eta,\zeta_m,\mu) = \Bigg[\Bigg( & \eta(\beta\delta\mu+\beta+\delta)\Omega^6 - 2\zeta_m(\beta+\delta)\Omega^5 - 2\eta\Big[\Big(\alpha^2(\mu\beta+\mu+1)\delta^2 + \big((\alpha^2+\frac{\mu}{2})\beta + \alpha^2 + \frac{\mu}{2} + \frac{1}{2}\big)\delta \\ & + \frac{\beta(\mu+1)}{2}\Big)\gamma^2 + \frac{\beta}{2} + \frac{\delta}{2}\Big]\Omega^4 - 2\gamma^2\zeta_m\Big[\alpha^2(\eta^2-1)\delta^2 + \big(-1+(\beta\eta^2+\eta^2-\beta-1)\alpha^2\big)\delta - \beta\Big]\Omega^3 \\ & + 2\gamma^2\eta\Big[\alpha^2\delta^2 + \Big(\frac{1}{2} + \big((\mu\beta+\mu+1)\gamma^2+\beta+1\big)\alpha^2\Big)\delta + \frac{\beta}{2}\Big]\Omega^2 + 2\alpha^2\delta\eta^2\gamma^4\zeta_m\Omega - 2\alpha^2\delta\gamma^4\zeta_m\Omega \\ & - 2\alpha^2\delta\eta\gamma^4\Big)\Bigg]^2 \end{aligned}$$

## Appendix B Fatigue life-cycle analysis of the flexural-hinges

A schematic view of a semi-circular flexural-hinge used in this study is given in Figure 7 (b). The maximum stress tends to occur in the thinnest section of the flexural-hinge, whose fatigue strength is reduced by different factors [50, 55]. The stress concentration factor, the effective stress concentration factor (as discussed in [56]), and the surface roughness factor are considered in the fatigue analysis while the thermal effects are neglected. The allowable stress amplitude $S_a$ is also a function of the mean stress $\sigma_m$ at the notch and can be given with the Goodman criteria for general use [50, 55] as

$$S_a = S_f\left(1 - \frac{\sigma_m}{S_U}\right), \tag{B.1}$$

where $S_f$ is the fatigue strength obtained from a smooth standard test specimen without notch and $S_U$ is the ultimate tensile strength of the material used. After applying the reduction factors, Equation B.1 can be rewritten as [55]

$$S_a = \frac{\gamma_s S_f}{K_e}\left(1 - \frac{\sigma_m}{S_U/K_t}\right), \tag{B.2}$$

where $K_t$, $K_e$ and $\gamma_s$ are the stress concentration factor, the effective stress concentration factor and the surface roughness reduction factor, respectively.

The maximum thickness of a notch for a given angular displacement is estimated by Smith [50], considering the maximum stress at the thinnest section of the notch to be

$$t_{max} = \frac{9\pi^2 R}{K_t^2 E^2 16}\left(\frac{\sigma}{\theta}\right)^2, \tag{B.3}$$

where $K_t$ is the stress concentration factor, which can be expressed as

$$K_t = (1+\beta_n)^{9/20}, \tag{B.4}$$

where $\beta_n$ is a dimensionless parameter, which equals $\beta_n = t/2R$. From Equation B.3, the maximum stress at the notch yields for a given thickness and radius of the notch

$$\sigma_{max} = \sqrt{\frac{16K_t^2E^2t}{9\pi^2R}}\theta, \tag{B.5}$$

where $\theta$ is the angular displacement of the flexural notch as expressed in Equation 14 and the relative displacement between the terminals of the inerter can be calculated from the equations of motion in Equation 7.

The accuracy of the theoretically obtained maximum stress in Equation B.5 was also compared with finite element analysis conducted in ANSYS Workbench. In the analysis, only one flexural hinge was considered and a equivalent rotational displacement to the relative displacement between the terminals of the pivoted-bar inerter was applied to the flexural hinge. The maximum stress occurred at the thinnest section of the notch as expected and the maximum stress values were found very close to theoretical estimations obtained from Equation B.5. For the parameters in Table 3 and 1 mm relative displacement between the inerter's terminals, theoretical estimation for the maximum stress was found as 246.6 MPa, while it was obtained 248.3 MPa from the finite element analysis in ANSYS Workbench as shown in Figure B.1 (a). The theoretical estimation and the finite element results for other relative displacement values were found to be very close.

The ratio of the allowable stress given to the maximum stress which occurs at the notch gives the safety factor of the notch hinge as

$$\text{Safety Factor} = \frac{S_a}{\sigma_{max}}. \tag{B.6}$$

The bending fatigue strength of Aluminium alloy 6082 T6/T651 for 100 million cycles and the surface roughness reduction factor for the flexural notches were assumed to be 130 MPa for an ultimate tensile strength of 340 MPa, and 0.75 for wire eroding manufacturing of Aluminium alloy as discussed in [55]. The effective stress concentration factor $K_e$ was calculated from $K_t$ using the notch sensitivity which is described as

$$q = \frac{K_e - 1}{K_t - 1}. \tag{B.7}$$

The notch sensitivity was taken to be 0.91 for the notch radius of 4.75 mm and Aluminium alloy as stated in [56].

In order to evaluate the fatigue life of the flexural notches for 100 million cycles, the safety factor is demonstrated in Figure B.1 (b) for the relative displacement between the terminals of the inerter whose distance $l_{bar} = 80$ mm. The safety factors for the relative displacement between the terminals of the inerter are given for the notch thicknesses of 0.1 and 0.5 assuming zero mean stress and mean stress of 50 MPa. Safety factors for the maximum stresses obtained from ANSYS Workbench were also indicated in Figure B.1 (b) for only zero mean stress.

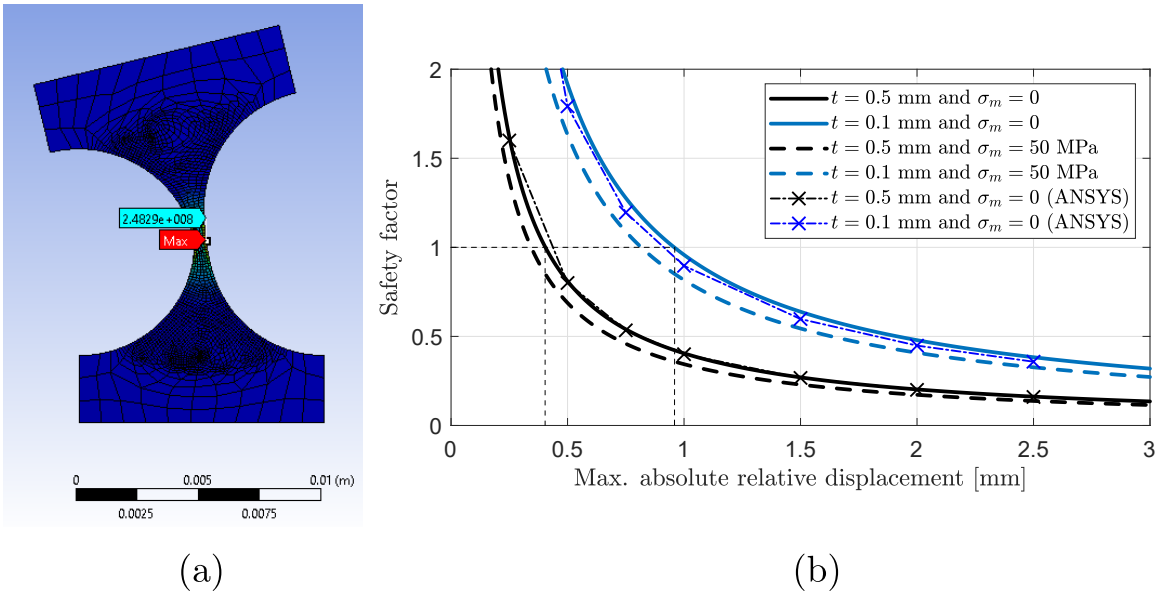


**Figure B.1**: (a) Maximum stress of the flexural hinge obtained from ANSYS Workbench and (b) fatigue life-cycle analysis of the flexure notch for the relative displacement between the terminals of the inerter device for $\sigma_m = 0$ and $\sigma = 50$ MPa.

It can be assumed that the flexural notches with a thickness of 0.5 mm can safely operate until 100 million cycles under relative displacement of the terminals of the inerter of 410 $\mu$m. For inerters that have higher relative displacements between their terminals, the notch thickness can be decreased, or the distance between the terminals can be increased as the maximum stress $\sigma_{max}$ is inversely proportional to the distance between the terminals i.e. $\theta = \frac{x_1 - x_2}{l_{bar}/2}$ as presented in Equation 14. Alternatively, a different material such as steel could be used instead of aluminium to increase the fatigue life but it should be considered that the high Young's Modulus of the steel will increase the stiffness of the flexural notch. This will shift the effective working frequency of the inerter design to the higher frequencies as explained in Figure 8.

## References


[1] M. Smith, Synthesis of mechanical networks: The inerter, in: Proceedings of the 41st IEEE Conference on Decision and Control, IEEE, pp. 1657–1662.

[2] D. J. Wagg, A review of the mechanical inerter: historical context, physical realisations and nonlinear applications, Nonlinear Dynamics (2021) 1–22.

[3] A. Okumura, The gyro-mass inerter, Japan Patent Koukai. H09-177 875, 1997.

[4] H. Kuroda, F. Arima, K. Baba, Y. Inoue, Principles and characteristics of viscous damping devices (gyro-damper), the damping forces which are highly amplified by converting the axial movement to rotary one, in: 12th WCEE.

[5] K. Saito, K. Yogo, Y. Sugimura, S. Nakaminami, K. Park, Application of rotary inertia to displacement reduction for vibration control system, in: 13th World Conference on Earthquake Engineering.

[6] K. Ikago, K. Saito, N. Inoue, Seismic control of single-degree-of-freedom structure using tuned viscous mass damper, Earthquake Engineering and Structural Dynamics 41 (2012) 453–474.

[7] I. F. Lazar, S. A. Neild, D. J. Wagg, Using an inerter-based device for structural vibration suppression, Earthquake Engineering and Structural Dynamics 43 (2014) 1129–1147.

[8] J. Hartog D., Ormondroyd, The theory of the dynamic vibration absorber, Journal of Applied Mechanics (1928) 49–50.

[9] Y. Hu, C. Z. Q. Chen, Michael, Z. Shu, L. Huang, Analysis and optimisation for inerter-based isolators via fixed-point theory and algebraic solution, Journal of Sound and Vibration 346 (2015) 17–36.

[10] L. Marian, A. Giaralis, Optimal design of a novel tuned mass-damper-inerter (tmdi) passive vibration control configuration for stochastically support-excited structural systems, Probabilistic Engineering Mechanics 38 (2014) 156–164.

[11] L. Marian, A. Giaralis, The tuned mass-damper-inerter for harmonic vibrations suppression, attached mass reduction, and energy harvesting, Smart Structures and Systems 19 (2017) 665–678.

[12] M. De Angelis, A. Giaralis, F. Petrini, D. Pietrosanti, Optimal tuning and assessment of inertial dampers with grounded inerter for vibration control of seismically excited base-isolated systems, Engineering Structures 196 (2019) 109250.

[13] D. Pietrosanti, M. De Angelis, A. Giaralis, Experimental study and numerical modeling of nonlinear dynamic response of SDOF system equipped with tuned mass damper inerter (TMDI) tested on shaking table under harmonic excitation, International Journal of Mechanical Sciences 184 (2020) 105762.

[14] Y. Hu, M. Z. Q. Chen, Performance evaluation for inerter-based dynamic vibration absorbers, International Journal of Mechanical Sciences 99 (2015) 297–307.

[15] E. Barredo, A. Blanco, J. Colin, V. M. Penagos, A. Abundez, L. G. Vela, V. Meza, R. H. Cruz, J. Mayen, Closed-form solutions for the optimal design of inerter-based dynamic vibration absorbers, International Journal of Mechanical Sciences 144 (2018) 41–53.

[16] S. Zhou, C. Jean-Mistral, S. Chesne, Optimal design of an inerter-based dynamic vibration absorber connected to ground, Journal of Vibration and Acoustics, Transactions of the ASME 141 (2019) 1–11.

[17] E. Barredo, M. J. G. Larios, J. Colin, J. Mayen, A. A. Flores-Hernandez, M. Arias-Montiel, A novel high-performance passive non-traditional inerter-based dynamic vibration absorber, Journal of Sound and Vibration 485 (2020) 115583.

[18] A. Giaralis, F. Petrini, Wind-induced vibration mitigation in tall buildings using the tuned mass-damper-inerter, Journal of Structural Engineering 143 (2017).

[19] K. Xu, K. Bi, Q. Han, X. Li, X. Du, Using tuned mass damper inerter to mitigate vortex-induced vibration of long-span bridges: Analytical study, Engineering Structures (2019) 101–111.

[20] A. Giaralis, A. A. Taflanidis, Optimal tuned mass-damper-inerter (TMDI) design for seismically excited MDOF structures with model uncertainties based on reliability criteria, Structural Control and Health Monitoring 25 (2017) 1–22.

[21] K. Ikago, Y. Sugimura, K. Saito, N. Inoue, Seismic displacement control of multiple-degree-of-freedom structures using tuned viscous mass dampers, in: G. De Roeck, G. Degrande, G. Lombaert, G. Muller (Eds.), Proceedings of the 8th International Conference on Structural Dynamics, EURODYN 2011, Leuven, Belgium, pp. 1800–1807.

[22] M. C. Smith, F.-C. Wang, Performance benefits in passive vehicle suspensions employing inerters, Vehicle Dynamics 42 (2004) 235–257.

[23] Y. Hu, J. Wang, C. Z. Q. Chen, Michael, Z. Li, Y. Sun, Load mitigation for a barge-type floating offshore wind turbine via inerter-based passive structural control, Engineering Structures 177 (2018) 198–209.

[24] R. Zhang, Z. Zhao, K. Dai, Seismic response mitigation of a wind turbine tower using a tuned parallel inerter mass system, Engineering Structures 180 (2019) 29–39.

[25] C. Papageorgiou, N. E. Houghton, M. C. Smith, Experimental testing and analysis of inerter devices, Journal of Dynamic Systems, Measurement, and Control, Transaction of the ASME 131 (2009) 1–11.

[26] Y. Hu, M. Z. Q. Chen, Z. Shu, Passive vehicle suspensions employing inerters with multiple performance requirements, Journal of Sound

and Vibration 333 (2014) 2212–2225.
[27] Y. Shen, L. Chen, X. Yang, D. Shi, J. Yang, Improved design of dynamic vibration absorber by using the inerter and its application in vehicle suspension, Journal of Sound and Vibration 361 (2015) 148–158.
[28] J. Z. Jiang, M. C. Smith, H. N. E, Experimental testing and modelling of a mechanical steering compensator, in: 3rd International Symposium on Communications, Control, and Signal Processing ISCCSP, pp. 249–254.
[29] F.-C. Wang, M.-F. Hong, W.-C. Chen, Building suspensions with inerters, in: Proc. IMechE Vol.224 Part C: J. Mechanical Engineering Science, pp. 1605–1616.
[30] S. Y. Zhang, J. Z. Jiang, N. Simon, Optimal configurations for a linear vibration suppression device in a multi-storey building, Structural Control and Health Monitoring 24 (2017) 1–17.
[31] D. De Domenico, P. Deastra, G. Ricciardi, N. D. Sims, D. J. Wagg, Novel fluid inerter based tuned mass dampers for optimised structural control of base-isolated buildings, Journal of the Franklin Institute 356 (2019) 7626–7649.
[32] Y. Li, J. Z. Jiang, S. A. Neild, Optimal inerter-based shock-strut configurations for landing-gear touchdown performance, Journal of Aircraft 54 (2017) 1901–1909.
[33] J. Z. Jiang, A. Z. Matamoros-Sanchez, R. M. Goodall, M. C. Smith, Passive suspensions incorparating inerters for railway vehicles, Vehicle System Dynamics 50 (2012) 263–276.
[34] F.-C. Wang, M.-F. Hong, T.-C. Lin, Designing and testing a hydraulic inerter, Journal of Mechanical Engineering Science 225 (2010) 66–72.
[35] M. Lazarek, P. Brzeski, P. Perlikoswki, Design and identification of parameters of tuned mass damper with inerter which enables changes of inertance, Mechanism and Machine Theory 119 (2018) 161–173.
[36] R. Ma, K. Bi, H. Hao, A novel rotatinonal inertia damper for amplifying fluid resistance: Experiment and mechanical model, Mechanical Systems and Signal Processing 149 (2021) 107313.
[37] M. Z. Chen, C. Papageorgiou, F. Scheibe, F.-C. Wang, M. C. Smith, The missing mechanical circuit element, IEEE Circuits and Systens Magazine 9 (2009) 10–26.
[38] M. C. Smith, The Inerter: A Retrospective, Annual Review of Control, Robotics, and Autonomous Systems 3 (2020) 361–391.
[39] F. C. Wang, W. J. Su, Impact of inerter nonlinearities on vehicle suspension control, Vehicle System Dynamics 46 (2008) 575–595.
[40] X. Liu, B. Titurus, J. Z. Jiang, Generalisable model development for fluid-inerter integrated damping devices, Mechanism and Machine Theory 137 (2019) 1–22.
[41] E. D. A. John, D. J. Wagg, Design and testing of a frictionless mechanical inerter device using living-hinges, Journal of the Franklin Institute 356 (2019) 7650–7668.
[42] P. Deastra, D. Wagg, N. Sims, M. Akbar, Tuned inerter dampers with linear hysteretic damping, Earthquake Engineering and Structural Dynamics 49 (2020) 1216–1235.
[43] D. J. Mead, The control of vibration by localized additions, in: Passive Vibration Control, John Wiley & Sons, 1999, pp. 267–317.
[44] H. Dogan, N. D. Sims, D. J. Wagg, The effects of parasitic mass on the performance of inerter-based dynamic vibration absorbers, in: 11th International Conference on Structural Dynamics, EURODYN, volume 1, pp. 1545–1555.
[45] J. A. Inaudi, N. Makris, Time-domain analysis of linear hysteretic damping, Earthquake Engineering and Structural Dynamics 25 (1996) 529–545.
[46] A. Qin, P. Suganthan, Self-adaptive Differential Evolution Algorithm for Numerical Optimization, 2005 IEEE Congress on Evolutionary Computation 2 (2005) 1785–1791.
[47] K. Worden, G. Manson, On the identification of hysteretic systems. Part I: Fitness landscapes and evolutionary identification, Mechanical Systems and Signal Processing 29 (2012) 201–212.
[48] W. Flannelly, Dynamic Antiresonant Vibration Isolator, US Patent. 3 322 379, 1967.
[49] S. S. Rao, Semidefinite systems, in: Mechanical Vibrations, Pearson, 5th edition, 2011, pp. 497–500.
[50] S. T. Smith, Flexures: Elements of elastic mechanisms, CRC Press, 2000.
[51] A. Almagirby, J. A. Rongong, M. J. Carre, The development of a new artificial model of a finger for assessing trasmitted vibrations, Journal of the Mechanical Behavior of Biomedical Materials 78 (2018) 20–27.
[52] A. Almagirby, J. A. Rongong, M. J. Carré, The development of a new artificial model of a finger for assessing transmitted vibrations, Journal of the Mechanical Behavior of Biomedical Materials 78 (2018) 20–27.
[53] A. Almagirby, Understanding Vibration Transmitted to the Human Finger, Ph.D. thesis, 2016.
[54] D. N. Tasron, Understanding the tribological interactions between plantar skin and sock textiles through the development of biofidelic test-beds, Ph.D. thesis, 2017.
[55] F. Dirksen, M. Anselmann, T. I. Zohdi, R. Lammering, Incorporation of flexural hinge fatigue-life cycle criteria into the topological design of compliant small-scale devices, Precision Engineering 37 (2013) 531–541.
[56] W. D. Pilkey, Notch sensitivity, in: Peterson's Stress Concetration Factors, John Wiley - Sons, 2 edition, 1997, pp. 36–40.